
Article:
Li, Z., Xiong, W., Hooper, A. orcid.org/0000-0003-4244-6652 et al. (6 more authors) (2025) Imaging viscosity after the 2021 Mw 7.4 Maduo earthquake: Insights on the regional rheology variation beneath the Bayan Har block. Earth and Planetary Science Letters, 666. 119465. ISSN: 0012-821X

https://doi.org/10.1016/j.epsl.2025.119465

Imaging Viscosity After The 2021 Mw 7.4 Maduo Earthquake: Insights On The Regional Rheology Variation Beneath The Bayan Har Block

Zhen Li[1,2], Wei Xiong[3], Andrew Hooper[2], Zeyan Zhao[1], Yuan Gao[2, 4], John R. Elliott[2], Tim J. Wright[2], Han Yue[1], Teng Wang[1*]

1. School of Earth and Space Sciences, Peking University, Beijing, China

2.COMET, Institute of Geophysics and Tectonics, School of Earth and Environment, University of Leeds, UK

3. Key Laboratory of Seismic Observation and Geophysical Imaging, Institute of Seismology, China Earthquake Administration, Wuhan, China

4. School of Environment and Spatial Informatics, China University of Mining and Technology, Xuzhou, China

Abstract:

The rheology of Earth's lithosphere fundamentally governs tectonic processes and landscape evolution. Postseismic deformation following large earthquakes has been widely used to constrain rheological structures globally. However, regional-scale rheological variations remain poorly understood due to the infrequency of large earthquakes. The Bayan Har Block in the central-eastern Tibetan Plateau is a unique tectonic unit to investigate rheology regional-variations by pronounced high seismicity, high heat flow anomalies, and localized lithospheric thinning. Here, we image postseismic deformation following the 2021 Maduo earthquake using InSAR and GNSS observations to probe the rheology over the block's north-east margin. We integrate long-term and short-term interferograms to separate deformation from atmospheric signals. After accounting for interseismic velocity, InSAR measurements extends out to 200 km from the rupture and its tips. Compared with prior studies, higher-quality far-field measurements allow the separation of viscoelastic relaxation from near-field afterslip effects. Our preferred model indicates a Burgers (bi-viscous) lower-crust rheology with transient and steady-state viscosities of $2.5^{+2.5}_{-1.3}\times10^{18}$ Pa·s and $2.5^{+0.7}_{-0.5}\times10^{19}$ Pa·s, respectively, beneath a 20-km-thick elastic layer. By testing laterally-variable and depth-dependent rheological structures, we identify a smaller viscosity contrast across the Jiangcuo Fault (factor of ~2) than that observed after the 2008 Wenchuan (factor of ~10) and 2001 Kokoxili (factor of ~5) earthquakes. This result suggests a positive correlation between viscosity contrasts, fault slip rates, and topographic gradients at a regional scale. These findings highlight that the rheological contrasts within the Bayan Har block exert a fundamental control on the long-term topographic evolution of the central Tibetan Plateau.

Highlights:

- We separate the spatial-temporal domains of afterslip and viscoelastic relaxation by leveraging high-quality InSAR and GNSS data.
- Our optimal model suggests lateral variable rheological structures exist within the Bayan Har block.
- This study provides a large-scale crustal rheological model, revealing a positive correlation between viscosity contrasts, fault slip rates, and topographic gradients.

Key words:
Bayan Har block, Postseismic deformation, Rheology, Viscosity Contrast, InSAR, GNSS

1. Introduction

Our knowledge of lower crust rheology is primarily inferred from geophysical observations probing the subsurface (Chen and Molnar, 1981; Yin and Harrison, 2000), rock experiments, and geological observations of analogues (Getsinger et al., 2013; Kenis et al., 2005). Following the development of space geodetic methods such as Global Navigation Satellite System (GNSS) and Interferometric Synthetic Aperture Radar (InSAR), surface deformation following large earthquakes and loading changes have been widely used to constrain the rheology of the lower crust directly (Avouac, 2015; Elliott et al., 2016) revealing the variations of the viscosity of the lower crust at a global scale (Fang et al., 2024; Shen et al., 2001). Such variations are fundamental in modulating the kinematics of plate tectonics and mantle convection (Coltice et al., 2017). However, the determination of lower crust rheology strongly depends on stress perturbations from large earthquakes, which occur infrequently. Consequently, regional-scale insights into rheological variations across diverse crustal properties remain scarce, hindering the refinement of geodynamic models connecting deep-Earth properties with landscape evolution (Ding et al., 2022).

Situated in the central-eastern Tibetan Plateau, the Bayan Har block is an ideal and critical region for probing the regional rheology variation, given its high levels of seismic activity in the instrumental era (Liu et al., 2006). The Bayan Har block, bounded by the Qaidam Basin to the northwest and the Sichuan Basin to the east, is flanked by the strike-slip systems of the Kunlun Fault to the north and the Ganzi-Yushu-Xianshuihe Fault to the south (Zhang et al., 2004). These major faults accommodate the crustal stress loading through variable slip rates

of 5–15 mm/yr, directly linked to the high seismic activities. Since 1990, most of China's significant continental earthquakes occurred around the Bayan Har block, including the 1997 M_w 7.6 Manyi, 2001 M_w 7.8 Kokoxili, 2008 M_w 7.9 Wenchuan, 2010 M_w 6.9 Yushu, and 2021 M_w 7.4 Maduo earthquakes (see the references in Table S3, S4). These earthquakes and their postseismic deformation, have been extensively studied with geodetic measurements, and the resulting viscous models provide constraints for the regional rheology beneath the Bayan Har block and across its major boundary faults. Estimated lower crustal viscosities from these earthquakes range from ~4×10^{19} Pa·s in the northwest to ~5×10^{18} Pa·s in the southeast, suggesting a possible first-order spatial decrease across the eastern Tibetan Plateau. Across boundary faults, the lower-crustal viscosities within the Qaidam Basin are approximately 2 times higher than those within the Bayan Har block, while in the Sichuan Basin are up to 20 times greater (Figure 1). Besides, geodetically constrained viscous models have shown that contrasts in lithospheric strength can localize strain along major faults (Jin et al., 2024). This supports earlier geodynamic interpretations where strong crustal blocks deflect deformation into weaker regions, promoting uplift and thickening (Beaumont et al., 2001; Wang, M et al., 2008). These observations motivate a key question: do spatial variations in rheology control fault slip partitioning and the development of plateau topography?

This question is particularly important for the Kunlun Fault system, which exhibits a well-documented west-to-east decrease in slip rates—from ~10 mm/yr near the 2001 Kokoxili rupture to ~5 mm/yr near the 2021 Maduo earthquake (Diao et al., 2019). This variation may reflect spatial variations in lithospheric strength, suggesting that rheological heterogeneity influences how slip is distributed along major faults (Fang et al., 2024). However, the rheological structure beneath the East Kunlun Fault remains poorly constrained, while the 2021 M_w 7.4 Maduo earthquake provides an opportunity to reveal it. Following the earthquake, published models have either focused on single mechanisms such as afterslip or shear zones (Fang et al., 2022; Jin and Fialko, 2021; Xiong et al., 2022) or integrated multiple processes into combined frameworks, including viscoelastic relaxation, afterslip and poroelastic rebound (Chen et al., 2024; Jin et al., 2023; Tang et al., 2023; Tian et al., 2024). Yet the literature lacks a separate evaluation of individual deformation mechanisms, which is essential for identifying the specific processes responsible for distinct deformation features. The main challenge is distinguishing the mechanically coupled viscoelastic flow from deep afterslip, spanning the first several years after the earthquake, as encountered in many other cases (Pollitz et al., 2021). Therefore, the inferred effective viscosities and upper crustal

thicknesses differ considerably, with values ranging from 10^{18} to 10^{20} Pa·s and 15 to 35 km, respectively. Moreover, deeper structural contrasts, as suggested by regional variations in topography and slip rates, are not captured by models in literature. This underscores the need for further studies that disentangle the effects of individual postseismic mechanisms and incorporate three-dimensional rheological variations.

Far-field geodetic observations are crucial for isolating viscoelastic relaxation separately, as it is less contaminated by near-field mechanisms like afterslip and poroelastic. However, previous studies used InSAR data that were either limited to ~50 km from the fault, had low signal-to-noise ratios, or offered broad coverage but neglected error correction, making them inadequate for capturing subtle far-field deformation (Jin et al., 2023; Tian et al., 2024). Wide-range GNSS networks have been proven to help distinguish the mechanisms, particularly far from the rupture and beyond the rupture tips (Hearn, 2003). Unfortunately, the sparse GNSS coverage, even when supplemented with InSAR, often struggles to capture these millimetre-scale, hundred-kilometre-wavelength signals during the early postseismic stage. The large-scale InSAR measurements are easily obscured by atmospheric noise, interseismic deformation, and systematic errors. Previous studies encountered two primary challenges: 1) a failure to account for obvious interseismic slip along the Kunlun Fault system and 2) the limited spatial coverage and low signal-to-noise ratios of GNSS and InSAR data. Viscosity estimates derived from low-quality observations often fail to accurately represent the rheological structure, particularly under the underestimation of elastic layer thickness (Jin et al., 2023; Tian et al., 2024). Therefore, effectively constraining the effects of multiple mechanisms separately requires longer-period, high-quality, full-field InSAR postseismic displacements with accounting for the interseismic contribution and atmospheric delay.

Here, we aim to assess the separate effects originating from deep afterslip and viscoelastic relaxation in the early stage after the 2021 Maduo earthquake, using data constraints from 6 tracks of Sentinel-1 SAR images and 23 continuous GNSS stations. The high-quality, far-field measurements, effectively excluding near-field afterslip effects, allow us to constrain the rheological structures. To our knowledge, this is the first instance of providing direct far-field InSAR observations that delineate the distinct spatial-temporal domains of afterslip and viscoelastic relaxation during the early postseismic phase. After testing different settings for a suite of viscoelastic models, we uncover the viscosity contrast across the Jiangcuo Fault and

the regional-scale variations beneath the Bayan Har Block, with implications for the potential influence on fault activity and landscape evolution.

2. Geodetic observations

2.1 GNSS measurements

The early postseismic deformation is recorded by GNSS stations from 23 continuous sites, ranging from near the fault to approximately 500 km away (Figure 2). This network, deployed and operated by the China Earthquake Administration, provides comprehensive coverage of the affected area. The processed position time series reveal clear postseismic transients combined with steady interseismic deformation, seasonal variations, and other factors (Hong and Liu, 2021). For isolating the postseismic deformation, we employ the affine-invariant ensemble sampler for Markov chain Monte Carlo (Foreman-Mackey et al., 2013) to estimate the optimal parameters using a logarithmic decay model , described as (Freed, 2007; Hong and Liu, 2021):

$$\mathrm{F} = \mathrm{V}_0 \times (t - to) + a_1 \times \log\left(1 + \frac{t - t_0}{\tau}\right)$$

$$+a_2 \cos(2\pi t) + a_3 \sin(2\pi t) + a_4 \cos(4\pi t) + a_5 \sin(4\pi t) + a_6 \,,$$

where t_0 is the earthquake occurrence time, V_0 is the regional secular velocity of GNSS stations, a_1 represents the amplitude of the logarithmic term, indicating a gradual change over time, and τ is the characteristic relaxation time, controlling the rate of this logarithmic change. a_2 through a_5 describe the seasonal components: the first pair representing annual seasonal variations, while the second represent higher-frequency semi-annual seasonal variations. Finally, a_6 is the constant term, representing the baseline level of the function. See details in the Text S2 & Figure S1. We exclude the vertical components of the GNSS data due to large errors relative to the signal. The cumulative deformation over 2.5 years, inferred from the optimal parameters, demonstrate a generally symmetrical pattern moving away from either side of the fault. The maximum east-west displacement reaches approximately 6 cm near the fault, with a decay coefficient of 10 days, reducing to a millimetre level beyond 200 km from the epicentre (Figure 2).

2.2 InSAR data processing

To map the localized and distributed deformation induced by the 2021 Maduo earthquake, we process six tracks of Sentinel-1 SAR images, including Ascending Tracks AT099, AT172, and AT26, and Descending Tracks DT106, DT033, and DT004, covering the period from pre-seismic to 2.5-year postseismic. We conduct SAR interferometry using a burst-based processing chain

implemented in the Sentinel-1 Interferometry Processor (Jiang et al., 2017). We employ the 90m Shuttle Radar Topography Mission Digital Elevation Model (Farr et al., 2007) to remove reference phases and for coregistration. All interferograms are multi-looked by factors of 23 in range and 6 in azimuth, yielding a resolution of approximately 125 × 125 m. Additionally, we process L-band ALOS-2 SAR images (AT149 and DT42 using ScanSAR mode) spanning the mainshock. We utilize both interferometry and pixel-offset tracking techniques for Sentinel-1 and ALOS-2 images in both azimuth and range directions to provide precise constraints for coseismic modelling.

For extracting low-amplitude, long-wavelength postseismic displacement induced by viscoelastic relaxation using InSAR, it is crucial to remove the contribution of atmospheric signal, interseismic displacement, and long-wavelength errors. First, we employ both the Generic Atmospheric Correction Online Service (GACOS) (Yu et al., 2018) and a common-scene stacking approaches (Tymofyeyeva and Fialko, 2015) to address atmospheric delays. The latter proves more effective in removing regional turbulence due to limited density of GNSS stations in Maduo area (Figure S3). Following the workflow shown in Figure S4, we first stack short-term interferograms with a common reference image with baselines within 180 days (Figure S5-S6) to estimate atmospheric delay. For recovering nonlinear signals, we apply a variable low-pass temporal filter by gradually reducing the number of stacked interferograms as the mainshock is approached, which is equivalent to time windows from 180 days to 24 days. Subsequently, we correct the long-term interferograms (around 1 or 2 years) with the estimated atmospheric phase before unwrapping. Second, we calculate the interseismic velocity from Sentinel-1 data over 7 years before the earthquake (Figure S2). The results indicate that interseismic deformation is characterized by long-wavelength tectonic features, with magnitudes increasing from north to south. A significant left-lateral deformation gradient is observed across the Kunlun Fault, highlighting the necessity of removing this component from postseismic deformation. Finally, we select an undeforming region (>400 km away from the rupture) unaffected by stress perturbations as a reference for variance weighting when stacking long-term interferograms. Finally, we correct long-wavelength ramps estimated from the undeforming region (Figures S7–S8). This comprehensive approach effectively enhances the signal-to-noise ratio of subtle postseismic displacement measurements, particularly in the far field.

To validate the determined postseismic deformation, we conduct a series of analyses and tests. Firstly, we test our short-term stacking strategy on simulated time series with power-law decay superimposed by random and seasonal noise. The resulting estimated time series closely reproduce the simulated data (Figure S9), indicating the robustness of our approach. Secondly, we compare our method with published observations from processing with Small Baseline Subset (SBAS) (Fang et al., 2022) and common scene stacking (Jin et al., 2023) and DetrendInSAR (Liu et al., 2024). The results show that our proposed methodology reproduces the long-wavelength and low-amplitude far-field deformation pattern with highest signal-to-noise ratio (Figure S10). Thirdly, we apply the same long-term stacking strategy to the GNSS time series to estimate the accumulated displacement. This estimation closely aligns with the InSAR-derived accumulated displacement, showing a discrepancy of no more than 1 mm/year (Figure S11). Finally, there is a high degree of consistency between the sampled InSAR-measured and GNSS-measured accumulated deformation (Figure 3). Collectively, these tests validate the reliability of our methodology in processing widely distributed postseismic deformation.

3. Coseismic source model of the 2021 Maduo earthquake

We infer the source model of the 2021 Maduo earthquake from down-sampled InSAR measurements using the Geodetic Bayesian Inversion Software (GBIS) (Bagnardi and Hooper, 2018) for fault geometry and the Steepest Descent Method (SDM) for slip distribution (Wang et al., 2011) (details in the supplementary). We divide the rupture into eight segments, fixing fault locations and strike angles based on field-mapped ruptures (Liu-Zeng et al., 2024). All the parameters are well constrained, according to their post-prior probability distributions (Figure S12). The inverted fault geometries show that segments S1–S6 dip northward with near-vertical angles, matching the distribution of relocated aftershocks north of the surface rupture, while segments S7 and S8 remain vertical due to the observed aftershock patterns. Based on the derived fault geometry, we invert for the slip distribution (Figure S13-15), which is mostly concentrated at depths of 5-10 km (Figure 1b). This result is in line with models from geodesy, seismic waveform inversion, and measured surface ruptures (Fang et al., 2022; He et al., 2021; Zhao et al., 2021). The peak slip of 6m occurred on segments S4 and S5, close to the seismically-derived epicentre at a depth of ~6 km (Figure 1). This earthquake induced a cumulative coseismic stress change of about 1 MPa in the lower crust (Figure 3a).

3. Mechanisms driving the postseismic deformation following the 2021 Maduo earthquake

The InSAR and GNSS measurements reveal a nearly a symmetrical "butterfly" pattern with an amplitude of approximately 5 cm in the line-of-sight (L0S) direction, extending over 200 km laterally in a direction normal to the surface rupture. In near field, prominent large-amplitude, short-wavelength signals dominate, likely caused by aftershocks, liquefaction, and shallow aseismic afterslip. We decompose the InSAR L0S observations into east-west and up-down deformation, assuming that the north-south deformation is negligible given the left-lateral mechanism (Figure 3). The east-west component highlights areas of maximum horizontal displacement, reaching up to ±6 cm, while the vertical component is up to ±2 cm. This decomposition confirms that the postseismic deformation is broadly distributed with regional vertical component.

We investigate several mechanisms that might contribute to the observed deformation, utilizing both time series of GNSS data and accumulated InSAR data over 2.5 years. We consider contributions from end-member models of each mechanism, including afterslip, viscoelastic relaxation, and poroelastic rebound. To determine the optimal parameter sets, we calculate the reduced Chi-Square value between predicted and observed deformation (details in the supplementary materials). After testing a few combinations of these mechanisms, we propose a combined model that best fits the geodetic observations for further interpretation.

3.1 Poroelastic rebound

The poroelastic rebound can cause measurable surface displacements hat are detectable through space geodetic observations (Jónsson et al., 2003). To evaluate the influence, we model the displacements under fully-drained and undrained conditions. Assuming pore fluid diffusion occurs at depths less than 15 km, we apply Poisson's ratios of 0.21 for drained and 0.27 for undrained conditions. Our model predicts several tens of millimetres of LOS deformation with lobes of opposite polarity at the rupture tips (Figure S16). However, the InSAR data do not exhibit such predicted displacement patterns above the noise threshold (10-20 mm), even if we do observe some localized vertical deformation, likely related to localized hydrology-induced processes. While poroelastic rebound may contribute to early near-field deformation (e.g., Tang et al., 2023), our drained–undrained model comparison shows it is limited to areas near the fault and does not match the observed pattern. Given our focus on long-term, far-field signals, its impact on interpreting viscoelastic relaxation and afterslip is minimal, as also suggested in other studies (Jin et al., 2023).

3.2 Afterslip

3.2.1 Kinematic inversions

We infer that afterslip occurred on and around the fault plane surrounding the coseismic ruptures. As demonstrated by previous studies, a spatial-temporal correlation between afterslip and aftershocks exists (Perfettini et al., 2018). The relocated aftershocks are concentrated at depths ranging from 0 to 30 km, suggesting that the downdip propagation of afterslip extends to a depth of 30 km (Figure S17). We extend the fault plane along the strike direction and downdip to 30 km following geologically identified Jiangcuo Fault traces (Pan et al., 2022). We perform the kinematic afterslip inversion using the SDM. To minimize inversion uncertainty, the rake angle is fixed at zero to only allow left-lateral strike-slip afterslip. The optimal model reveals a clear anti-correlation with the coseismic slip distribution, with maximum afterslip reaching approximately 0.6 m (Figure 4a). The afterslip is broadly distributed on the fault sections deeper than the seismogenic layer, which may exhibit more "velocity-strengthening" behaviour (Kaneko et al., 2008). The predicted deformation shows a relatively good fit to the near-to-middle field data within ~200 km. However, it underestimates the far-field observations, especially to the east of the rupture, and deviates from the observed symmetric pattern (Figure3).

To assess the potential role of afterslip in the lower crust, we extended the fault geometry along strike by 100 km and downdip to 60 km depth (Figure S19), producing a slip distribution that reasonably matches geodetic observations (Figures S19-20). While deep afterslip could, in theory, explain some of the deformation, its inclusion must be supported by geological and physical evidence. Below the brittle–ductile transition, stress is more likely accommodated by viscoelastic flow or distributed ductile shearing rather than continued frictional slip. In our study area, seismic imaging beneath the Jiangcuo Fault does not reveal a well-developed ductile shear zone, suggesting a lower crust dominated by viscous behavior (see Section 4.4). Furthermore, the along-strike extension of the fault is not supported by geological-documented faut trace and aftershock distributions (Figure 4D). Taken together, these findings support the interpretation that far-field postseismic deformation is primarily governed by viscoelastic relaxation, with stress in the lower crust more likely released through viscous flow than by deep afterslip.

3.2.2 Stress-driven down-dip extending afterslip

In kinematic inversions, while a rough fit to observations may be achieved, the inferred slip distribution lacks physical constraints (Figure 4a). The stress-driven afterslip model can be used to verify whether the slip amplitude and distribution are consistent with the relaxation of coseismic stress changes on a fault plane. Assuming steady-state rate-strengthening fault, the initial velocity driven by the coseismic stress change can be expressed by:

$$\mathrm{V} = 2V_0 \sinh\left(\frac{\Delta\tau}{\sigma(a-b)}\right)$$

where V_0 is a reference slip rate, $\Delta\tau$ is the coseismic shear stress change, (a-b) is the rate-and-state frictional parameter (Dieterich, 1979), and σ is the effective normal stress on the fault. We calculate the initial velocity distribution on the same fault geometry. To model stress-driven afterslip, we assume a homogeneous steady-state slip rate before the earthquake. For each pair of trial parameters $\sigma(a-b)$ and V_0, we compute the initial slip rate after the earthquake using the steady-state rate-and-state friction relation under the coseismic stress perturbation. The time-dependent evolution of afterslip is then simulated using a boundary integral method (Zhao and Yue, 2023).

To fit the GNSS time series, we explore a wide range of model parameters, i.e., V_0 and $\sigma(a-b)$, while considering only strike-direction afterslip. We set $\sigma(a-b)$ to 6 MPa for patches at 5 km depth to prevent unphysical large velocities in the upmost crust. Using a grid-search method, the determined optimal parameters are $V_0 = 4 \times 10^{-9}$ m/s, and for patches below 5 km, $\sigma(a-b)$ = 0.6 MPa. Assuming an effective normal stress of 100 MPa, this yields an estimate of $a = 6 \times 10^{-3}$, which is about one magnitude higher than the typical values of approximately 10^{-4} to 10^{-3} determined by laboratory experiments (Mitchell et al., 2016). The afterslip distribution patterns of the stress-driven and kinematic models are roughly consistent. However, differences appear at the two ends of the segments, such as S1, S7, and S8, suggesting that the inverted afterslip in these segments might be an artifact caused by other mechanisms (Figure 3). Furthermore, the predicted deformation aligns well with near-field displacements (Figure 6), however, the model significantly underestimates the deformation in far field, especially to the east of the rupture. This discrepancy highlights the need to incorporate additional viscoelastic relaxation to capture the far-field deformation.

3.3 Viscoelastic relaxation

We simulate the viscoelastic relaxation induced by the coseismic stress change using the open-source software Relax (Barbot and Fialko, 2010). Our vertically-stratified ductile lithospheric layer model, comprising the upper elastic layer, a viscoelastic lower crust, and an elastic half-

space upper mantle, is derived from the shear velocity model for the lithosphere beneath eastern Tibet (Li et al., 2024; Xiao et al., 2024), which suggests a weak layer characterized by low S-wave velocity in the mid-to-lower crust beneath the Bayan Har Block. Additionally, significant Moho depth variations, ranging from approximately 68 km to 45 km, are observed within the basin-mountain transition zone of the Kunlun Mountain-Qaidam Basin, indicating heterogeneous viscous structure across the Tibetan plateau. We justify the increase in complexity of our model setting by progressing from a Maxwell to a Burgers model, primarily based on far-field observations (100 km from the fault and along rupture tips, Figure 2).

3.3.1 Maxwell rheological model

To model viscoelastic relaxation effectively, determining the depth of the brittle-ductile transition layer, i.e., the thickness of the elastic layer, is crucial due to the inherent trade-off between thickness and viscosity (Bürgmann and Dresen, 2008). Based on regional shear velocity model, we conduct a grid search with a linear Maxwell rheology applied to the lower crust with a fixed crustal thickness of 68 km. We vary the elastic layer thickness from 10 to 40 km and the viscosity from 10^{17} to 10^{21} Pa·s (Figure S18). The optimal parameters are an elastic layer thickness of 20 km and a viscosity of 1.6×10^{19} Pa·s (VR Model-1, Figure S21). The inferred elastic layer thickness is consistent with the seismogenic extent of historical earthquake ruptures and the models proposed by Chen et al., 2024 and Tang et al., 2023, but it is shallower than the model proposed by Jin et al., 2023 and Tian et al. (2024). We then search for the lower crust viscosities, fixing the elastic layer thickness at 20 km. The optimal model indicates that the lower crust viscosity is approximately 10^{19} Pa·s (Figure 5a). Overall, the optimal model can reproduce the orientation and amplitude of surface deformation, particularly for far-field observations (Figure 5c). However, it fails to replicate the transient high velocity and overestimates the long-term displacement (Figure 5g), suggesting that a variation of linear viscoelastic rheology, such as a Burgers (bi-viscous) rheology with non-linear surface response, may be required.

3.3.2 Burgers rheological model

The Burgers model, which integrates linear elastic (Maxwell) and viscous (Kelvin-Voigt) elements, effectively captures both short-term and long-term deformation, making it suitable for simulating complex, non-linear postseismic processes (Bürgmann and Dresen, 2008). This model is characterized by steady-state viscosity (η_s) and shear modulus (μ_M), as well as transient viscosity (η_K) and shear modulus (μ_K). The long-term shear modulus is represented

by $\mu_M\mu_K$ / (μ_M + μ_K), with an initial instantaneous modulus of μ_M, and a relaxation ratio, α, defined as $\mu_K/(\mu_M + \mu_K)$. This fixed value may introduce a bias in estimating long-term relaxation (Ryder et al., 2011). Hence, we adopt a consistent value of α equal to 2/3, aligning with previous studies on the northern Tibetan Plateau (Ryder et al., 2011).

We still adopt the same three-layer rheological structure but modify the lower crust to a Burgers body while retaining the upper mantle as a Maxwell body with a fixed viscosity of 10^{20} Pa·s. We perform a grid search with the viscosities for both η_s and η_k, in the ranges from 10^{18} to 10^{21} Pa·s. The refined model reveals transient viscosity $\eta_k = 2.5^{+2.5}_{-1.3} \times 10^{18}$ Pa·s and steady-state viscosity $\eta_m = 2.5^{+0.7}_{-0.5} \times 10^{19}$ Pa·s, with a ratio of $\eta_m / \eta_k = 10$, consistent with the expected range of 1-30. This model excellently predicts the deformation, manifesting a "butterfly" pattern that matches well with middle-to-far field observations, particularly to the east beyond the rupture tip (Figure 5d, f). However, it still underestimates deformation in near field, notably at sites MD01, MD03, and MD09 (Figure 5d, f, g).

When constraining the viscosity using near-to-middle-field observations (no more than 100 km from the ruptures) exclusively, the optimal model reveals a transient viscosity of 1 x 10^{18} Pa·s and a steady-state viscosity of 6.3 x 10^{18} Pa·s (Figure 5c). These parameter sets are consistent with published models constrained by observations covering the same area (Chen et al., 2024). This model accurately captures the rapidly decaying transient signals at near-to-middle station sites (MD01, MD03, MD09, QHMQ). However, it results in a significant overestimation of displacement for far-field observations, as illustrated in Figures 5e, 5f, and 5g. This overestimation in the far field suggests that the inferred low transient viscosity may be an artifact arising from the influence of transient afterslip effects. Although the Burgers model is effective in capturing the rapidly decaying transient deformation, it does not accurately represent deformation across both near and far fields simultaneously. This limitation indicates that neither afterslip nor viscoelastic relaxation alone can simultaneously explain the spatial-temporal patterns of the far- and near-field observation.

3.4 Combined model with two-step searching strategy

Individual mechanisms such as afterslip and viscoelastic relaxation have proven insufficient to reproduce observations spanning near- to far-field observations simultaneously. Therefore, a combined model incorporating afterslip and viscoelastic relaxation is required. By a set of tests, we neglect the interaction between these co-evolving processes as the minor contribution

(Details in the supplementary, Figure S22). We consider two sets of combined models: 1) combined afterslip and Maxwell viscoelasticity, and 2) combined afterslip and Burgers viscoelasticity. To separate different mechanisms, we firstly apply far-field (>50km) observation only to constrain the viscoelastic relaxation model. After removing the viscoelastic relaxation contribution from the GNSS measurements, we perform a grid search for the initial slip velocity (V_0) ranging from 0.1 x 10^{-9} to 1 x 10^{-9} m/s and the frictional parameter (σ(a-b)) ranging from 0.01 to 1 MPa in the stress-driven afterslip model. We find that only the combined-afterslip-Burgers model can fully explain the observed displacements (Figure6). The optimal solution suggests that η_k is 2.5 x 10^{18} Pa·s and η_m is 2.5 x 10^{19} Pa·s, V_0 is 0.3 x 10^{-9} m/s and $\sigma(a-b)$ is 0.15 MPa (Figure6 and Figure S23). Notably, we observe significant misfits at the QHMD site, located approximately 40 km north of the rupture, which is likely caused by surface processes possibly related to non-elastic behaviors (Figure 6c). Generally, this combined model significantly improves data fitting compared to models using only afterslip, only viscoelastic relaxation, or both afterslip and Maxwell viscoelastic relaxation, enabling the quantification of the contributions from these two combined mechanisms (Table S2).

3.5 Depth-dependent and lateral heterogenous rheology model

The lithosphere's significant geothermal gradient suggests strong vertical variations in viscosity, motivating the need for depth-dependent viscosity to accurately capture postseismic deformation (Moore and Parsons, 2015). Building on the depth-dependent viscosity model proposed by Yamasaki and Houseman for the 1997 Manyi earthquake (Yamasaki and Houseman, 2012a), and informed by laboratory-based measurements (Watts et al., 2013), we construct a simplified depth-dependent Burgers rheological model. In this model, the ductile lower crust is divided into five sub-layers, with effective viscosity decreasing from 1.6×10^{20} on the top to 6.3×10^{18} Pa·s to the bottom, while the elastic upper crust and upper mantle are assumed constant (Figure 7a). Over 2.5 years following the mainshock, our depth-dependent viscosity model reveals a similar spatial deformation pattern to that of a homogeneous viscosity model, though with a slightly reduced maximum in LOS direction (25 mm vs. 30 mm, respectively, Figure S24). Despite this difference in amplitude, we find that the homogeneous viscosity model is able to capture the first-order constraints on vertical variations in crustal viscosity.

Given the contrasting geological structure along the northeastern margin of the Bayan Har Block and the overestimation of deformation across the EKLF by the uniform rheological model (Figure 7b; Figure S25), we explore a series of laterally heterogeneous scenarios. These range from simple uniform models to those incorporating variations in elastic layer thickness (Figure 7, Models a–c) and lower crustal viscosity (Models d–e). To reduce parameter trade-offs, we fix the ratio of steady-state to transient viscosity at 10 in the Burgers model, based on the best-fit symmetric configuration. Among all tested cases, only the asymmetric model with increased viscosity north of the Jiangcuo Fault (Model-d) adequately captures the subdued far-field deformation (>50 km from the fault) and reduces the RMS misfit from 5.6 mm to 5.1 mm (Figure S25; Table S1). To highlight spatial patterns, we extract surface displacement along the D–D' profile (Figure 7b), which reveals discrepancies not evident in global RMS. Model-f, in particular, better reproduces the weak deformation north of the EKLF, reinforcing the need for lateral rheological variations. The effective viscosity north of the Jiangcuo Fault is estimated at 4.6×10^{19} Pa·s, compared to 2.5×10^{19} Pa·s to the south. Assuming a viscosity of 10^{20} Pa·s north to East Kunlun Fault (Liu et al., 2019; Tian et al., 2024), the viscosity contrast across the north-eastern margin of the Bayan Har Block is estimated to be ~2, which is smaller than that inferred across the EKLF and LMS fault zones (Diao et al., 2018; Liu et al., 2019; Zhao et al., 2023). We acknowledge that observational noise and model simplifications limit the precise resolution of viscosity contrast. Nevertheless, the northward increase in viscosity is robust. The remained overestimation south of the EKLF (Figure 7b), suggest that incorporating along-strike viscosity variations could improve future models.

4. Discussion

4.1 Far-field geodetic observation is the key to constraining rheology structure and viscosity

Separating contributions from afterslip and viscoelastic relaxation processes following large earthquakes is particularly challenging due to limited knowledge of *in situ* frictional and rheological properties of rocks, as well as the hydrological conditions below the brittle-ductile transition. GNSS time series provide critical constraints on viscosity (Tian et al., 2024; Wang et al., 2021). The far-field observations, particularly those extending along the strike direction from the rupture tips, are unlikely to be affected by afterslip, and thus are essential for constraining the deeper viscoelastic relaxation processes. However, the long-wavelength deformation induced by ductile flow, which is highly sensitive to the thickness of the elastic layer, remains challenging to resolve due to the sparse spatial coverage of GNSS stations (Zhu et al., 2024). In the absence of high-resolution far-field deformation, elastic layer thickness

may be biased as showed in Figure 8a. Guided by high-resolution far-field observations, we infer that the elastic layer thickness is 20 km, rather than 35 km inferred by GNSS observations alone (Tian et al., 2024). This estimate aligns closely with the seismogenic depth of both the Maduo and adjacent large earthquakes, and is consistent with the latest high-resolution China Seismological Reference Model (Li et al., 2024; Xiao et al., 2024). The accurate constraints on the elastic layer thickness can help resolve its trade-off with viscosity. Generally, for continental strike-slip faults overlying a relatively weak crust, high-quality, wide-coverage postseismic geodetic data, including InSAR and GNSS, are crucial for constraining the rheological structure.

Long-term and far-field observations are essential for accurately assessing viscoelastic effects, which have often been overlooked in previous studies. To justify this, we highlight the spatiotemporal areas of dominance for afterslip and viscoelastic relaxation based on the evolution of east-west deformation in 1.5 cm cumulative contours produced by our best-fit model (Figure 6b). Our results reveal that afterslip primarily contributes to surface deformation within approximately 50 km of the fault (about three times the seismological depth), whereas viscoelastic relaxation plays a dominant role in far-field deformation, with broader and more prolonged effects. Notably, this mechanism is most evident at the rupture tips, where the deformation extends more than 100 km along strike during the same period (Figure 6b). In the early postseismic phase, afterslip and viscoelastic relaxation contribute comparably to the near-field deformation (within 50 km of the fault, Figure 6c). However, studies relying solely on near-field data often lack robust far-field constraints, leading to an overestimation of deep afterslip and an underappreciation of viscoelastic relaxation. For example, considering viscoelastic relaxation's contribution near the fault, we estimate that σ(a-b) on the fault plane is 0.15 MPa, compared to an overestimated 0.6 MPa if the viscoelastic effect is neglected (Figure S26). Moreover, the lower viscosity derived from early-stage observations may stem from underestimating afterslip, as exemplified by the values of 10^{18} Pa·s reported by Jin et al., (2023) and Chen et al., (2024). Additionally, the viscosity of the lower crust estimated from very short-period observations often loses tight constraints due to the influence of poroelastic rebound or shallow afterslip, as highlighted by Tang et al., (2023). These discrepancies in spatial and temporal patterns enable a quantitative distinction between transient rheological effects and early afterslip.

4.2 Depth-dependent and lateral-variable rheology beneath the Bayan Har Block

Laboratory experiments on rock deformation indicate that effective viscosity is highly sensitive to variations in temperature, stress, mineral composition, and water content (Pan and Shao, 2022). These dependencies imply pronounced spatial heterogeneity in effective viscosity, both laterally and vertically. In extreme cases, crustal rheology can vary at kilometre scales, as observed in postseismic deformation following the 2016 M_w 7.1 Kumamoto earthquake, where localized and distributed deformation patterns reflect these fine-scale viscosity differences (Moore et al., 2017). Within the Bayan Har block, viscosity decreases progressively from north to south (Figure 7b), characterized by increased folding and numerous anticlines and synclines, as supported by seismic reflection profiles and surface geological mapping (Harrowfield and Wilson, 2005; Xu et al., 2014). Besides, our study suggests that the viscosity north of the Jiangcuo Fault is 1–2 times larger than that to the south, and the viscosity north of East Kunlun Fault is 2–3 times larger than that within the block, which offers fundamental insights into the degree of viscosity contrast across the north-eastern margin of the Bayan Har block.

On the other hand, in natural settings, crustal viscosity is inherently depth-dependent, exhibiting a linear or power-law decay with increasing depth rather than being constant throughout the crust (Yamasaki and Houseman, 2012b). Assuming a constant viscosity can lead to inaccuracies in surface deformation estimates, particularly in regions where the rheological properties vary substantially between the upper and lower crust. To address this, we apply a sub-layered ductile model where viscosity decreases from 1.6×10^{20} Pa·s at the top to 6.3×10^{18} Pa·s at the base of the ductile layer. While this approach captures broad trends, it may still overlook the continuous depth variations expected throughout the crust (Figure S23). Our combined model without sub-layers suggests a relatively firm high-viscosity upper mantle (10^{20} Pa·s) is overlain by a weaker lower crust (transient viscosity: 2.5×10^{18} Pa·s, steady-state viscosity: 2.5×10^{19} Pa·s) and a 20-km-thick elastic layer, consistent with the “Jelly Sandwich” model (Bürgmann and Dresen, 2008). Given the constraints of data fit and realistic viscosity ranges, our model, though simplified, offers a reasonable approximation of the actual continuous, depth-dependent viscosity distribution, effectively capturing regional rheological properties.

4.3 Consistency of contrasts from topography, fault slip rate, and lower crust rheology

The variation in lithospheric rheology governs the lateral growth and topographic variations of the Tibetan Plateau under the collision between the Indian Plate and the Eurasia Plate that

began ~55 Ma (Ding et al., 2022; Tapponnier et al., 2001). Such asymmetric rheological structures and viscosities have been identified across the eastern margin (Longmenshan Orogenic Belt and Sichuan Basin) from studies of the 2008 Wenchuan Earthquake (Wang et al., 2021), the northwest margin (Kunlun Fault and Qaidam Basin) from studies of 2001 Kokoxili earthquake (Liu et al., 2019), corresponding to the predicted topographic gradients where viscosity differences are most significant. However, topographic variations are relatively minor across the northeast margin, including the East Kunlun Fault and Jiangcuo Fault (Figure S23). Our heterogeneous rheological model demonstrates slight contrasts in either viscosity or elastic layer thickness across the northeast margin of Bayan Har Block. We compare the averaged topography change and viscosity contrasts across the boundary fault in terms of the 2001 Kokoxili, 2008 Wenchuan, 2010 Yushu, and 2021 Maduo earthquakes. Figure 8b–c suggests a possible first-order association between viscosity contrast and topographic gradient across block margins. Although the trend is weak and based on a limited number of events, it is consistent with regional geodynamic expectations. Rheological contrasts between adjacent blocks may influence the localization of crustal shortening and thickening. Over geological timescales, such processes can contribute to the uplift and morphological evolution of the plateau (Royden et al., 2008).

In terms of fault activity, slip rates along the boundary faults of the Bayan Har Block correlate positively with crustal viscosity contrasts (Figure 8b). Along the Kunlun Fault in the northern margin, the segment near the Kokoxili earthquake has the highest slip rate, at approximately 10 ± 2 mm/yr (Diao et al., 2019; Kirby et al., 2007), adjacent to the stable Qaidam Basin at low elevation (~3000 m), where higher viscosity contrasts are observed (Figure 8c). Eastward, slip rates decrease to ~5 mm/yr (Liu-Zeng et al., 2024; Pan et al., 2022) near the Maduo earthquake and dissipate toward the Longmenshan Fault, with strain dispersing over a broader area in regions of lower viscosity contrast (Kirby et al., 2007). In the southern margin, the Ganzi-Yushu- Xianshuihe Faults show comparable trends: near the Yushu earthquake, slip rates range from 6–8 mm/yr (Huang et al., 2015), corresponding to lower viscosity contrasts. Farther east, GNSS and InSAR data indicate fault slip rates of 10–12 mm/yr (Qiao and Zhou, 2021) approaching the eastern margin, where the largest viscosity contrasts are evident. Notably, viscosity heterogeneities alone do not fully explain the formation and dynamics of surface faults or topographic transitions along major strike-slip faults. Other essential processes, like dissipative heating, grain-size reduction, and fracturing, are required (Harris and Day, 1993; Sammis and Ben-Zion, 2008). However, it helps initiate strain localization,

576 which couples with additional mechanisms to influence fault activities and topography
577 evolution (Molnar and Dayem, 2010).
578
579 The spatial correlation between lithospheric rheology, fault slip rates, and topographic
580 gradients suggests that viscosity contrasts play a key role in localizing strain and guiding the
581 long-term deformation of the Tibetan Plateau (Figure 9). Variations in crustal strength
582 influence how shortening is partitioned across the lithosphere: strong, stable blocks such as
583 the Qaidam and Sichuan Basins tend to deflect strain toward adjacent weaker regions,
584 promoting crustal thickening and uplift within the plateau interior (Beaumont et al., 2001;
585 Royden et al., 2008). However, this relationship may also involve feedback. Progressive crustal
586 thickening and surface uplift can enhance thermal insulation and radiogenic heating,
587 potentially reducing lower-crustal viscosity over time (Hacker et al., 2014, 2000; Pysklywec
588 and Beaumont, 2004). The interplay between rheology and topography is thus best
589 interpreted as a coupled thermomechanical process. Although our current dataset does not
590 constrain the temporal sequence of these interactions, previous modeling studies
591 demonstrate that lateral viscosity contrasts can effectively focus deformation and contribute
592 to plateau growth. Further insights into this feedback will require thermomechanical modeling
593 combined with constraints on the crust's thermal and tectonic evolution.
594
595 **4.4 Alternative models**
596 In this study, we examine individual and combined postseismic mechanisms using InSAR and
597 GNSS observations from the first 2.5 years following the Maduo earthquake. For the afterslip
598 component, we assume a simplified frictional parameter distribution and exclude its
599 variations along the strike direction to reduce model complexity. The optimized stress-driven
600 afterslip model demonstrates a strong spatial correlation with aftershock seismicity (Figure
601 S16), assuming that the afterslip is governed by coseismic Coulomb failure stress (CFS) changes.
602 Our results show that the combined model effectively captures the observed deformation,
603 both in total amplitude and in the temporal evolution across near- to far-field distances. Some
604 on-fault residuals persist, likely due to the assumption of homogeneous friction parameters
605 or other on-fault postseismic processes. Therefore, we mask the on-fault deformation area
606 during parameter estimation to ensure that this homogeneous assumption accurately
607 quantifies the relative contributions of afterslip and viscoelastic relaxation.
608

For the viscoelastic relaxation, it could be argued that postseismic viscoelastic deformation primarily reflects the viscosity of narrow ductile shear zones beneath major faults rather than the broader crust (Yamasaki et al., 2014). However, deep afterslip extends into upper mantle fails to explain the observed far-field deformation. Besides, high-resolution seismic imaging does not reveal a distinct Moho offset beneath the intra-block Jiangcuo Fault (Li et al., 2024; Xiao et al., 2024), in contrast to the adjacent boundary faults, such as the Kunlun Fault and Xianshuihe Fault, which exhibit higher slip rates. Therefore, the geodetic and seismic observations do not support the idea that the Jiangcuo Fault develops into a deep shear zone that penetrates the full depth of the lithosphere. Our inferred effective viscosity of ~10^{19} Pa·s is consistent with that estimated from lake loading change (Fan et al., 2023; Henriquet et al., 2019), which reflects rheology of the broader lithosphere. We propose that the far-field deformation associated with the 2021 intra-block Maduo earthquake likely originates from a broader zone of ductile flow within the lower crust, though this should be discussed on a case-by-case basis, particularly for boundary faults. Notably, the corresponding characteristic relaxation time is estimated at about 10 years, which exceeds the current observation period. Since the effective viscosity tends to increase over time, our estimate serves as a lower bound on the long-term effective viscosity of the lower crust. Our estimated lower-crustal viscosity (~2.5×10^{19} Pa·s) is lower than the ~10^{21} Pa·s estimated from long-term GNSS and InSAR data, which reflects steady-state deformation and lithospheric strength over geological timescale (Fang et al., 2024). These differences highlight the temporal sensitivity of viscosity estimates. Both studies provide valuable insights, but they address distinct aspects of the rheology of the Tibetan Plateau, with our study offering a finer resolution of the short-term viscosity response.

5. Conclusions

We derive a comprehensive field of postseismic deformation spanning 2.5 years and approximately 1000 kilometres across the surface ruptures of the 2021 Madou earthquake, utilizing 6 tracks of Sentinel-1 SAR images and data from 23 continuous GNSS stations. The high-quality far-field measurements, effectively excluding near-field afterslip effects, allow us to constrain the rheological structures at depth. To our knowledge, this is the first study that delineates the distinct spatial-temporal domains of afterslip and viscoelastic relaxation by relying on high-quality far-field InSAR measurements during the early postseismic phase. By removing the interaction between afterslip and viscoelastic relaxation, the transient and steady-state modelled viscosities beneath the block interior are estimate to be $2.5^{+2.5}_{-1.3}\times10^{18}$ Pa·s and $2.5^{+0.7}_{-0.5}\times10^{19}$ Pa·s, respectively. Our model suggests a subtle asymmetry in the rheological

structure either side of the fault, and when considered alongside the pronounced viscosity contrasts in the Sichuan and Qaidam basins, provides evidence that viscosity variations may play a role in regional topographic evolution. This study provides new insights into determining crustal viscosities from early postseismic deformation imaged over a wide area, and reveals viscosity variations beneath the Bayan Har Block, along with their potential influence on topographic evolution and fault activity.

CRediT authorship contribution statement

Zhen Li: Conceptualization, Methodology, Formal analysis, Writing Original Draft, Funding acquisition; **Wei Xiong**: Data acquirement, Writing – Review & Editing; **Andrew Hooper**: Supervision, Project administration, Formal analysis, Writing – Review & Editing; Zeyan **Zhao:** Methodology, Formal analysis, Writing – Review & Editing; **Yuan Gao:** Formal analysis, Writing – Review & Editing; **John Elliott**: Formal analysis, Writing – Review & Editing. **Tim Wright**: Formal analysis, writing – Review & Editing; **Han Yue**: Methodology, Supervision, Writing – Review & Editing; **Teng Wang**: Conceptualization, Supervision, Project administration, Funding acquisition, Formal analysis, Writing – Review & Editing.

Declaration of competing interest

The authors declare that they have no known competing financial interests or personal relationships that could have appeared to influence the work reported in this paper.

Data Availability

The GNSS and InSAR data used in this paper are available at: https://doi.org/10.5281/zenodo.15273475

Acknowledgments

We thank all the seismologists and geodesists from previous generations who contributed to the establishment and measurement of the GNSS network across Tibetan Plateau. Sentinel-1 SAR data are provided by the European Space Agency and are additionally distributed by the Alaska Satellite Facility. We acknowledge the insightful discussion from Professor Sylvain Barbot, Roland Bürgmann, Gregory A. Houseman, and Dr. Jin Fang. This work is funded by the National Natural Science Foundation of China (42021003).

References

677 Avouac, J.-P., 2015. From Geodetic Imaging of Seismic and Aseismic Fault Slip to Dynamic
678 Modeling of the Seismic Cycle. Annu. Rev. Earth Planet. Sci. 43, 233–271.
679 https://doi.org/10.1146/annurev-earth-060614-105302
680 Bagnardi, M., Hooper, A., 2018. Inversion of Surface Deformation Data for Rapid Estimates
681 of Source Parameters and Uncertainties: A Bayesian Approach. Geochem. Geophys.
682 Geosystems 19, 2194–2211. https://doi.org/10.1029/2018GC007585
683 Barbot, S., Fialko, Y., 2010. A unified continuum representation of post-seismic relaxation
684 mechanisms: semi-analytic models of afterslip, poroelastic rebound and viscoelastic
685 flow. Geophys. J. Int. 182, 1124–1140. https://doi.org/10.1111/j.1365-
686 246X.2010.04678.x
687 Beaumont, C., Jamieson, R.A., Nguyen, M.H., Lee, B., 2001. Himalayan tectonics explained by
688 extrusion of a low-viscosity crustal channel coupled to focused surface denudation.
689 Nature 414, 738–742. https://doi.org/10.1038/414738a
690 Bürgmann, R., Dresen, G., 2008. Rheology of the Lower Crust and Upper Mantle: Evidence
691 from Rock Mechanics, Geodesy, and Field Observations. Annu. Rev. Earth Planet. Sci.
692 36, 531–567. https://doi.org/10.1146/annurev.earth.36.031207.124326
693 Chen, F., Diao, F., Haghighi, M.H., Wang, Y., Zhu, Y., Wang, R., Xiong, X., 2024. Mechanism
694 and implications of the post-seismic deformation following the 2021 Mw 7.4 Maduo
695 (Tibet) earthquake. Geophys. J. Int. 237, 203–216.
696 https://doi.org/10.1093/gji/ggae034
697 Chen, W.-P., Molnar, P., 1981. Constraints on the seismic wave velocity structure beneath
698 the Tibetan Plateau and their tectonic implications. J. Geophys. Res. Solid Earth 86,
699 5937–5962. https://doi.org/10.1029/JB086iB07p05937
700 Coltice, N., Gérault, M., Ulvrová, M., 2017. A mantle convection perspective on global
701 tectonics. Earth-Sci. Rev. 165, 120–150.
702 https://doi.org/10.1016/j.earscirev.2016.11.006
703 Diao, F., Wang, R., Wang, Y., Xiong, X., Walter, T.R., 2018. Fault behavior and lower crustal
704 rheology inferred from the first seven years of postseismic GPS data after the 2008
705 Wenchuan earthquake. Earth Planet. Sci. Lett. 495, 202–212.
706 https://doi.org/10.1016/j.epsl.2018.05.020
707 Diao, F., Xiong, X., Wang, R., Walter, T.R., Wang, Y., Wang, K., 2019. Slip Rate Variation Along
708 the Kunlun Fault (Tibet): Results From New GPS Observations and a Viscoelastic
709 Earthquake-Cycle Deformation Model. Geophys. Res. Lett. 46, 2524–2533.
710 https://doi.org/10.1029/2019GL081940
711 Ding, L., Kapp, P., Cai, F., Garzione, C.N., Xiong, Z., Wang, H., Wang, C., 2022. Timing and
712 mechanisms of Tibetan Plateau uplift. Nat. Rev. Earth Environ. 3, 652–667.
713 https://doi.org/10.1038/s43017-022-00318-4
714 Elliott, J.R., Walters, R.J., Wright, T.J., 2016. The role of space-based observation in
715 understanding and responding to active tectonics and earthquakes. Nat. Commun. 7,
716 13844. https://doi.org/10.1038/ncomms13844
717 Fan, W., Wang, T., Shi, X., 2023. Lower Crust Viscosity in Central Tibet Inferred From InSAR
718 Derived Deformation Around Siling Co Lake After Its Rapid Expansion in the 2000s.
719 Geophys. Res. Lett. 50, e2023GL104863. https://doi.org/10.1029/2023GL104863
720 Fang, J., Ou, Q., Wright, T.J., Okuwaki, R., Amey, R.M.J., Craig, T.J., Elliott, J.R., Hooper, A.,
721 Lazecký, M., Maghsoudi, Y., 2022. Earthquake Cycle Deformation Associated With
722 the 2021 MW 7.4 Maduo (Eastern Tibet) Earthquake: An Intrablock Rupture Event
723 on a Slow-Slipping Fault From Sentinel-1 InSAR and Teleseismic Data. J. Geophys.
724 Res. Solid Earth 127, e2022JB024268. https://doi.org/10.1029/2022JB024268
725 Fang, J., Wright, T.J., Johnson, K.M., Ou, Q., Styron, R., Craig, T.J., Elliott, J.R., Hooper, A.,
726 Zheng, G., 2024. Strain Partitioning in the Southeastern Tibetan Plateau From

727 Kinematic Modeling of High-Resolution Sentinel-1 InSAR and GNSS. Geophys. Res.
728 Lett. 51, e2024GL111199. https://doi.org/10.1029/2024GL111199
729 Farr, T.G., Rosen, P.A., Caro, E., Crippen, R., Duren, R., Hensley, S., Kobrick, M., Paller, M.,
730 Rodriguez, E., Roth, L., Seal, D., Shaffer, S., Shimada, J., Umland, J., Werner, M.,
731 Oskin, M., Burbank, D., Alsdorf, D., 2007. The Shuttle Radar Topography Mission.
732 Rev. Geophys. 45. https://doi.org/10.1029/2005RG000183
733 Foreman-Mackey, D., Hogg, D.W., Lang, D., Goodman, J., 2013. emcee: The MCMC Hammer.
734 Publ. Astron. Soc. Pac. 125, 306. https://doi.org/10.1086/670067
735 Freed, A.M., 2007. Afterslip (and only afterslip) following the 2004 Parkfield, California,
736 earthquake. Geophys. Res. Lett. 34. https://doi.org/10.1029/2006GL029155
737 Getsinger, A.J., Hirth, G., Stünitz, H., Goergen, E.T., 2013. Influence of water on rheology and
738 strain localization in the lower continental crust. Geochem. Geophys. Geosystems
739 14, 2247–2264. https://doi.org/10.1002/ggge.20148
740 Hacker, B.R., Ratschbacher, L., Webb, L., McWilliams, M.O., Ireland, T., Calvert, A., Dong, S.,
741 Wenk, H.-R., Chateigner, D., 2000. Exhumation of ultrahigh-pressure continental
742 crust in east central China: Late Triassic-Early Jurassic tectonic unroofing. J. Geophys.
743 Res. Solid Earth 105, 13339–13364. https://doi.org/10.1029/2000JB900039
744 Hacker, B.R., Ritzwoller, M.H., Xie, J., 2014. Partially melted, mica-bearing crust in Central
745 Tibet. Tectonics 33, 1408–1424. https://doi.org/10.1002/2014TC003545
746 Harris, R.A., Day, S.M., 1993. Dynamics of fault interaction: parallel strike-slip faults. J.
747 Geophys. Res. Solid Earth 98, 4461–4472. https://doi.org/10.1029/92JB02272
748 Harrowfield, M.J., Wilson, C.J.L., 2005. Indosinian deformation of the Songpan Garzê Fold
749 Belt, northeast Tibetan Plateau. J. Struct. Geol. 27, 101–117.
750 https://doi.org/10.1016/j.jsg.2004.06.010
751 He, K., Wen, Y., Xu, C., Zhao, Y., 2021. Fault Geometry and Slip Distribution of the 2021
752 Mw 7.4 Maduo, China, Earthquake Inferred from InSAR Measurements and
753 Relocated Aftershocks. Seismol. Res. Lett. 93, 8–20.
754 https://doi.org/10.1785/0220210204
755 Hearn, E.H., 2003. What can GPS data tell us about the dynamics of post-seismic
756 deformation? Geophys. J. Int. 155, 753–777. https://doi.org/10.1111/j.1365-
757 246X.2003.02030.x
758 Henriquet, M., Avouac, J.-P., Bills, B.G., 2019. Crustal rheology of southern Tibet constrained
759 from lake-induced viscoelastic deformation. Earth Planet. Sci. Lett. 506, 308–322.
760 https://doi.org/10.1016/j.epsl.2018.11.014
761 Hong, S., Liu, M., 2021. Postseismic Deformation and Afterslip Evolution of the 2015 Gorkha
762 Earthquake Constrained by InSAR and GPS Observations. J. Geophys. Res. Solid Earth
763 126, e2020JB020230. https://doi.org/10.1029/2020JB020230
764 Huang, X., Du, Y., He, Z., Ma, B., Xie, F., 2015. Late Quaternary slip rate of the Batang Fault
765 and its strain partitioning role in Yushu area, central Tibet. Tectonophysics 653, 52–
766 67. https://doi.org/10.1016/j.tecto.2015.03.026
767 Jiang, H., Feng, G., Wang, T., Bürgmann, R., 2017. Toward full exploitation of coherent and
768 incoherent information in Sentinel-1 TOPS data for retrieving surface displacement:
769 Application to the 2016 Kumamoto (Japan) earthquake. Geophys. Res. Lett. 44,
770 1758–1767. https://doi.org/10.1002/2016GL072253
771 Jin, Z., Fialko, Y., 2021. Coseismic and Early Postseismic Deformation Due to the 2021 M7.4
772 Maduo (China) Earthquake. Geophys. Res. Lett. 48, e2021GL095213.
773 https://doi.org/10.1029/2021GL095213
774 Jin, Z., Fialko, Y., Yang, H., Li, Y., 2023. Transient Deformation Excited by the 2021 M7.4
775 Maduo (China) Earthquake: Evidence of a Deep Shear Zone. J. Geophys. Res. Solid
776 Earth 128, e2023JB026643. https://doi.org/10.1029/2023JB026643

Jónsson, S., Segall, P., Pedersen, R., Björnsson, G., 2003. Post-earthquake ground movements correlated to pore-pressure transients. Nature 424, 179–183. https://doi.org/10.1038/nature01776

Kaneko, Y., Lapusta, N., Ampuero, J.-P., 2008. Spectral element modeling of spontaneous earthquake rupture on rate and state faults: Effect of velocity-strengthening friction at shallow depths. J. Geophys. Res. Solid Earth 113. https://doi.org/10.1029/2007JB005553

Kenis, I., Urai, J.L., van der Zee, W., Hilgers, C., Sintubin, M., 2005. Rheology of fine-grained siliciclastic rocks in the middle crust—evidence from structural and numerical analysis. Earth Planet. Sci. Lett. 233, 351–360. https://doi.org/10.1016/j.epsl.2005.02.007

Kirby, E., Harkins, N., Wang, E., Shi, X., Fan, C., Burbank, D., 2007. Slip rate gradients along the eastern Kunlun fault. Tectonics 26. https://doi.org/10.1029/2006TC002033

Li, S., Liu, T., Liu, C., Wang, Y., Lu, H.-Z., Xie, X.C., 2024. Progress on the antiferromagnetic topological insulator MnBi2Te4. Natl. Sci. Rev. 11, nwac296. https://doi.org/10.1093/nsr/nwac296

Liu, M., Mooney, W.D., Li, S., Okaya, N., Detweiler, S., 2006. Crustal structure of the northeastern margin of the Tibetan plateau from the Songpan-Ganzi terrane to the Ordos basin. Tectonophysics, Seismic Probing of Continents and their Margins 420, 253–266. https://doi.org/10.1016/j.tecto.2006.01.025

Liu, S., Xu, X., Klinger, Y., Nocquet, J.-M., Chen, G., Yu, G., Jónsson, S., 2019. Lower Crustal Heterogeneity Beneath the Northern Tibetan Plateau Constrained by GPS Measurements Following the 2001 Mw7.8 Kokoxili Earthquake. J. Geophys. Res. Solid Earth 124, 11992–12022. https://doi.org/10.1029/2019JB017732

Liu-Zeng, J., Liu, Z., Liu, X., Milliner, C., Rodriguez Padilla, A.M., Xu, S., Avouac, J.-P., Yao, W., Klinger, Y., Han, L., Shao, Y., Yan, X., Aati, S., Shao, Z., 2024. Fault Orientation Trumps Fault Maturity in Controlling Coseismic Rupture Characteristics of the 2021 Maduo Earthquake. AGU Adv. 5, e2023AV001134. https://doi.org/10.1029/2023AV001134

Mitchell, E.K., Fialko, Y., Brown, K.M., 2016. Velocity-weakening behavior of Westerly granite at temperature up to 600°C. J. Geophys. Res. Solid Earth 121, 6932–6946. https://doi.org/10.1002/2016JB013081

Molnar, P., Dayem, K.E., 2010. Major intracontinental strike-slip faults and contrasts in lithospheric strength. Geosphere 6, 444–467. https://doi.org/10.1130/GES00519.1

Moore, J.D.P., Parsons, B., 2015. Scaling of viscous shear zones with depth-dependent viscosity and power-law stress–strain-rate dependence. Geophys. J. Int. 202, 242–260. https://doi.org/10.1093/gji/ggv143

Moore, J.D.P., Yu, H., Tang, C.-H., Wang, T., Barbot, S., Peng, D., Masuti, S., Dauwels, J., Hsu, Y.-J., Lambert, V., Nanjundiah, P., Wei, S., Lindsey, E., Feng, L., Shibazaki, B., 2017. Imaging the distribution of transient viscosity after the 2016 Mw 7.1 Kumamoto earthquake. Science 356, 163–167. https://doi.org/10.1126/science.aal3422

Pan, J., Li, H., Chevalier, M.-L., Tapponnier, P., Bai, M., Li, Chao, Liu, F., Liu, D., Wu, K., Wang, P., Li, Chunrui, Lu, H., Chen, P., 2022. Co-seismic rupture of the 2021, Mw7.4 Maduo earthquake (northern Tibet): Short-cutting of the Kunlun fault big bend. Earth Planet. Sci. Lett. 594, 117703. https://doi.org/10.1016/j.epsl.2022.117703

Pan, P.-Z., Shao, C.-Y., 2022. Experimental studies on the physical and mechanical properties of heated rock by air, water and high-viscosity fluid cooling. Geomech. Energy Environ. 31, 100315. https://doi.org/10.1016/j.gete.2022.100315

Perfettini, H., Frank, W.B., Marsan, D., Bouchon, M., 2018. A Model of Aftershock Migration Driven by Afterslip. Geophys. Res. Lett. 45, 2283–2293. https://doi.org/10.1002/2017GL076287

827 Pysklywec, R.N., Beaumont, C., 2004. Intraplate tectonics: feedback between radioactive
828 thermal weakening and crustal deformation driven by mantle lithosphere
829 instabilities. Earth Planet. Sci. Lett. 221, 275–292. https://doi.org/10.1016/S0012-
830 821X(04)00098-6
831 Qiao, X., Zhou, Y., 2021. Geodetic imaging of shallow creep along the Xianshuihe fault and its
832 frictional properties. Earth Planet. Sci. Lett. 567, 117001.
833 https://doi.org/10.1016/j.epsl.2021.117001
834 Royden, L.H., Burchfiel, B.C., van der Hilst, R.D., 2008. The Geological Evolution of the
835 Tibetan Plateau. Science 321, 1054–1058. https://doi.org/10.1126/science.1155371
836 Ryder, I., Bürgmann, R., Pollitz, F., 2011. Lower crustal relaxation beneath the Tibetan
837 Plateau and Qaidam Basin following the 2001 Kokoxili earthquake. Geophys. J. Int.
838 187, 613–630. https://doi.org/10.1111/j.1365-246X.2011.05179.x
839 Sammis, C.G., Ben-Zion, Y., 2008. Mechanics of grain-size reduction in fault zones. J.
840 Geophys. Res. Solid Earth 113. https://doi.org/10.1029/2006JB004892
841 Shen, F., Royden, L.H., Burchfiel, B.C., 2001. Large-scale crustal deformation of the Tibetan
842 Plateau. J. Geophys. Res. Solid Earth 106, 6793–6816.
843 https://doi.org/10.1029/2000JB900389
844 Tang, X., Guo, R., Xu, J., Zheng, Y., 2023. Role of Poroelasticity and Viscoelasticity during the
845 Postseismic Deformation of the 2021 Mw 7.4 Maduo, China, Earthquake. Seismol.
846 Res. Lett. https://doi.org/10.1785/0220230060
847 Tapponnier, P., Zhiqin, X., Roger, F., Meyer, B., Arnaud, N., Wittlinger, G., Jingsui, Y., 2001.
848 Oblique Stepwise Rise and Growth of the Tibet Plateau. Science 294, 1671–1677.
849 https://doi.org/10.1126/science.105978
850 Tian, Z., Freymueller, J.T., He, Y., Ji, G., Wang, S., Li, Z., 2024. Postseismic deformation due to
851 the 2021 MW 7.4 Maduo (China) earthquake and implications for regional rheology
852 and seismic hazards around the Bayan Har block. Earth Planet. Sci. Lett. 647, 119059.
853 https://doi.org/10.1016/j.epsl.2024.119059
854 Tymofyeyeva, E., Fialko, Y., 2015. Mitigation of atmospheric phase delays in InSAR data, with
855 application to the eastern California shear zone. J. Geophys. Res. Solid Earth 120,
856 5952–5963. https://doi.org/10.1002/2015JB011886
857 Wang, M., Shen, Z.-K., 2020. Present-Day Crustal Deformation of Continental China Derived
858 From GPS and Its Tectonic Implications. J. Geophys. Res. Solid Earth 125,
859 e2019JB018774. https://doi.org/10.1029/2019JB018774
860 Wang, M., Shen, Z.-K., Wang, Y.-Z., Bürgmann, R., Wang, F., Zhang, P.-Z., Liao, H., Zhang, R.,
861 Wang, Q., Jiang, Z.-S., Chen, W.-T., Hao, M., Li, Y., Gu, T., Tao, W., Wang, K., Xue, L.,
862 2021. Postseismic Deformation of the 2008 Wenchuan Earthquake Illuminates
863 Lithospheric Rheological Structure and Dynamics of Eastern Tibet. J. Geophys. Res.
864 Solid Earth 126, e2021JB022399. https://doi.org/10.1029/2021JB022399
865 Wang, R., Schurr, B., Milkereit, C., Shao, Z., Jin, M., 2011. An Improved Automatic Scheme for
866 Empirical Baseline Correction of Digital Strong-Motion Records. Bull. Seismol. Soc.
867 Am. 101, 2029–2044. https://doi.org/10.1785/0120110039
868 Watts, A.B., Zhong, S.J., Hunter, J., 2013. The Behavior of the Lithosphere on Seismic to
869 Geologic Timescales. Annu. Rev. Earth Planet. Sci. 41, 443–468.
870 https://doi.org/10.1146/annurev-earth-042711-105457
871 Xiao, X., Cheng, S., Wu, J., Wang, W., Sun, L., Wang, X., Ma, J., Tong, Y., Liang, X., Tian, X., Li,
872 H., Chen, Q.-F., Yu, S., Wen, L., 2024. CSRM-1.0: A China Seismological Reference
873 Model. J. Geophys. Res. Solid Earth 129, e2024JB029520.
874 https://doi.org/10.1029/2024JB029520
875 Xiong, W., Chen, W., Wang, D., Wen, Y., Nie, Z., Liu, G., Dijin, W., Yu, P., Qiao, X., Zhao, B.,
876 2022. Coseismic slip and early afterslip of the 2021 Mw 7.4 Maduo, China

earthquake constrained by GPS and InSAR data. Tectonophysics 840, 229558. https://doi.org/10.1016/j.tecto.2022.229558

Xu, T., Wu, Z., Zhang, Z., Tian, X., Deng, Y., Wu, C., Teng, J., 2014. Crustal structure across the Kunlun fault from passive source seismic profiling in East Tibet. Tectonophysics, Advances in seismic imaging of crust and mantle 627, 98–107. https://doi.org/10.1016/j.tecto.2013.11.010

Yamasaki, T., Houseman, G.A., 2012a. The crustal viscosity gradient measured from post-seismic deformation: A case study of the 1997 Manyi (Tibet) earthquake. Earth Planet. Sci. Lett. 351–352, 105–114. https://doi.org/10.1016/j.epsl.2012.07.030

Yamasaki, T., Houseman, G.A., 2012b. The signature of depth-dependent viscosity structure in post-seismic deformation. Geophys. J. Int. 190, 769–784. https://doi.org/10.1111/j.1365-246X.2012.05534.x

Yamasaki, T., Wright, T.J., Houseman, G.A., 2014. Weak ductile shear zone beneath a major strike-slip fault: Inferences from earthquake cycle model constrained by geodetic observations of the western North Anatolian Fault Zone. J. Geophys. Res. Solid Earth 119, 3678–3699. https://doi.org/10.1002/2013JB010347

Yin, A., Harrison, T.M., 2000. Geologic Evolution of the Himalayan-Tibetan Orogen. Annu. Rev. Earth Planet. Sci. 28, 211–280. https://doi.org/10.1146/annurev.earth.28.1.211

Yu, C., Li, Z., Penna, N.T., Crippa, P., 2018. Generic Atmospheric Correction Model for Interferometric Synthetic Aperture Radar Observations. J. Geophys. Res. Solid Earth 123, 9202–9222. https://doi.org/10.1029/2017JB015305

Zhang, P.-Z., Shen, Z., Wang, M., Gan, W., Bürgmann, R., Molnar, P., Wang, Q., Niu, Z., Sun, J., Wu, J., Hanrong, S., Xinzhao, Y., 2004. Continuous deformation of the Tibetan Plateau from global positioning system data. Geology 32, 809–812. https://doi.org/10.1130/G20554.1

Zhao, D., Qu, C., Chen, H., Shan, X., Song, X., Gong, W., 2021. Tectonic and Geometric Control on Fault Kinematics of the 2021 Mw7.3 Maduo (China) Earthquake Inferred From Interseismic, Coseismic, and Postseismic InSAR Observations. Geophys. Res. Lett. 48, e2021GL095417. https://doi.org/10.1029/2021GL095417

Zhao, D., Qu, C., Shan, X., Bürgmann, R., Chen, H., Wu, D., Gong, W., 2023. Post-seismic deformation of the 2008 Wenchuan earthquake reveals a misaligned rheological boundary in the lower crust along the eastern Tibetan Plateau margin. Geophys. J. Int. 235, 1353–1372. https://doi.org/10.1093/gji/ggad304

Zhao, Z., Yue, H., 2023. A two-step inversion for fault frictional properties using a temporally varying afterslip model and its application to the 2019 Ridgecrest earthquake. Earth Planet. Sci. Lett. 602, 117932. https://doi.org/10.1016/j.epsl.2022.117932

Zhu, Y., Wang, K., Xie, S., Jiang, Y., Zhou, X., 2024. Dominance of transient rheology in far-field postseismic deformation following the 2012 Mw 7.8 Haida Gwaii and 2013 Mw 7.5 Craig earthquakes. Earth Planet. Sci. Lett. 636, 118698. https://doi.org/10.1016/j.epsl.2024.118698

Figures

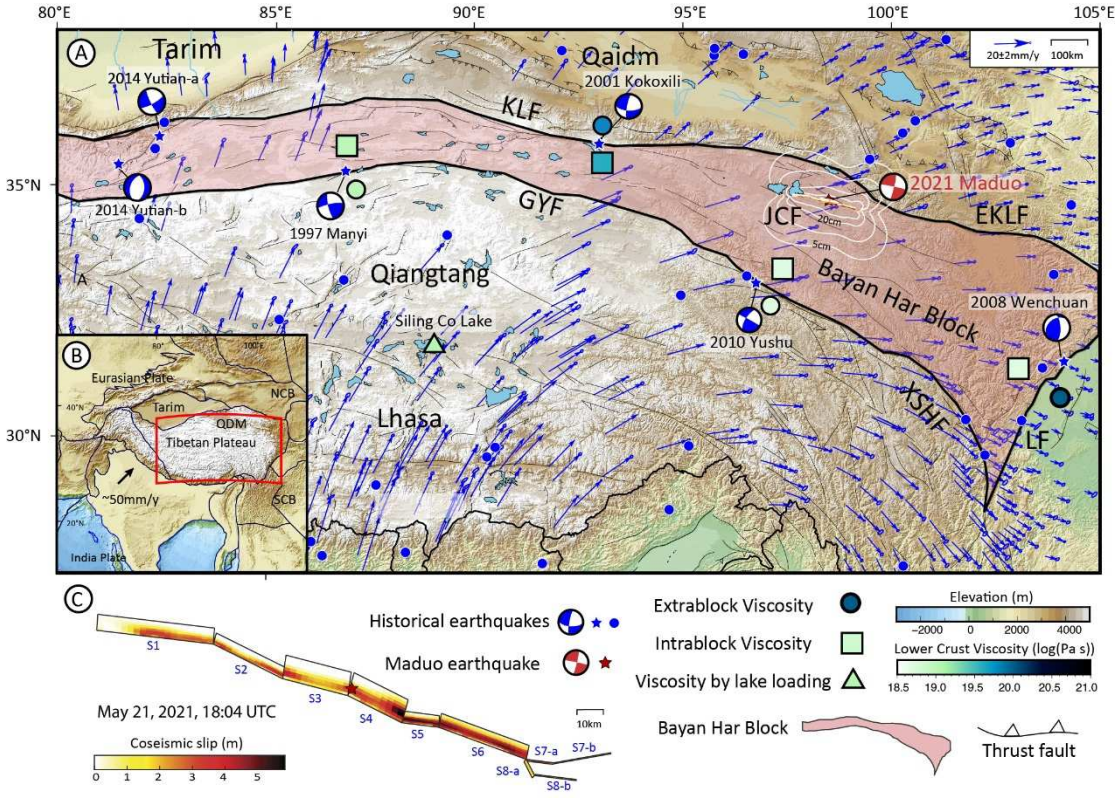

Figure 1: Tectonic setting of the Bayan Har Block with recent destructive earthquakes. (A) Elevation map of the study area with key tectonic and geophysical features. Blue-coloured rectangles indicate viscosity values corresponding to those listed in Table S4. Blue dots indicate historical earthquakes, while red dots represent the 2021 Madou Earthquake. GPS stations are indicated by red squares. Blue vectors are GPS-derived velocities from M. Wang & Shen, 2020. The Bayan Kala Block is shaded in pink, with major faults labelled as KLF (Kunlun Fault), EKLF (Eastern Kunlun Fault), and XSHF (Xianshuihe Fault). (B)The inset map shows the regional tectonic setting, illustrating the interaction between the Eurasian Plate, Indian Plate, and Tibetan Plateau. (C) Coseismic slip distribution

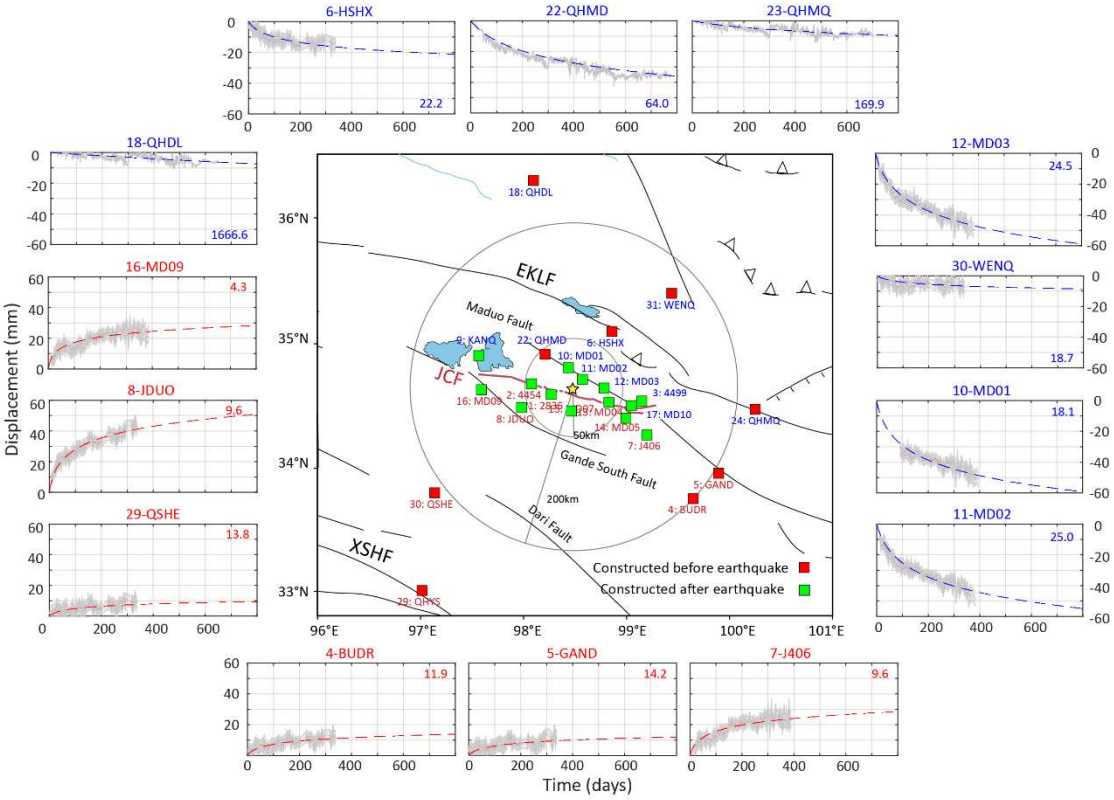

Figure 2: Distribution of GNSS sites with time-series deformation. The central map depicts the spatial distribution of the GNSS stations used in the analysis, with red squares indicating stations constructed before the earthquake and green squares for those constructed after the earthquake. The yellow circle represents the epicentre. Surrounding the map, individual time series plots show the deformation recorded at each station over time (in days after the Maduo earthquake). Stations north of the rupture, showing fitted decreasing deformation trends (westward motion), are represented with blue dashed lines, while those south of the rupture, showing increasing trends (eastward motion), are marked with red dashed lines.

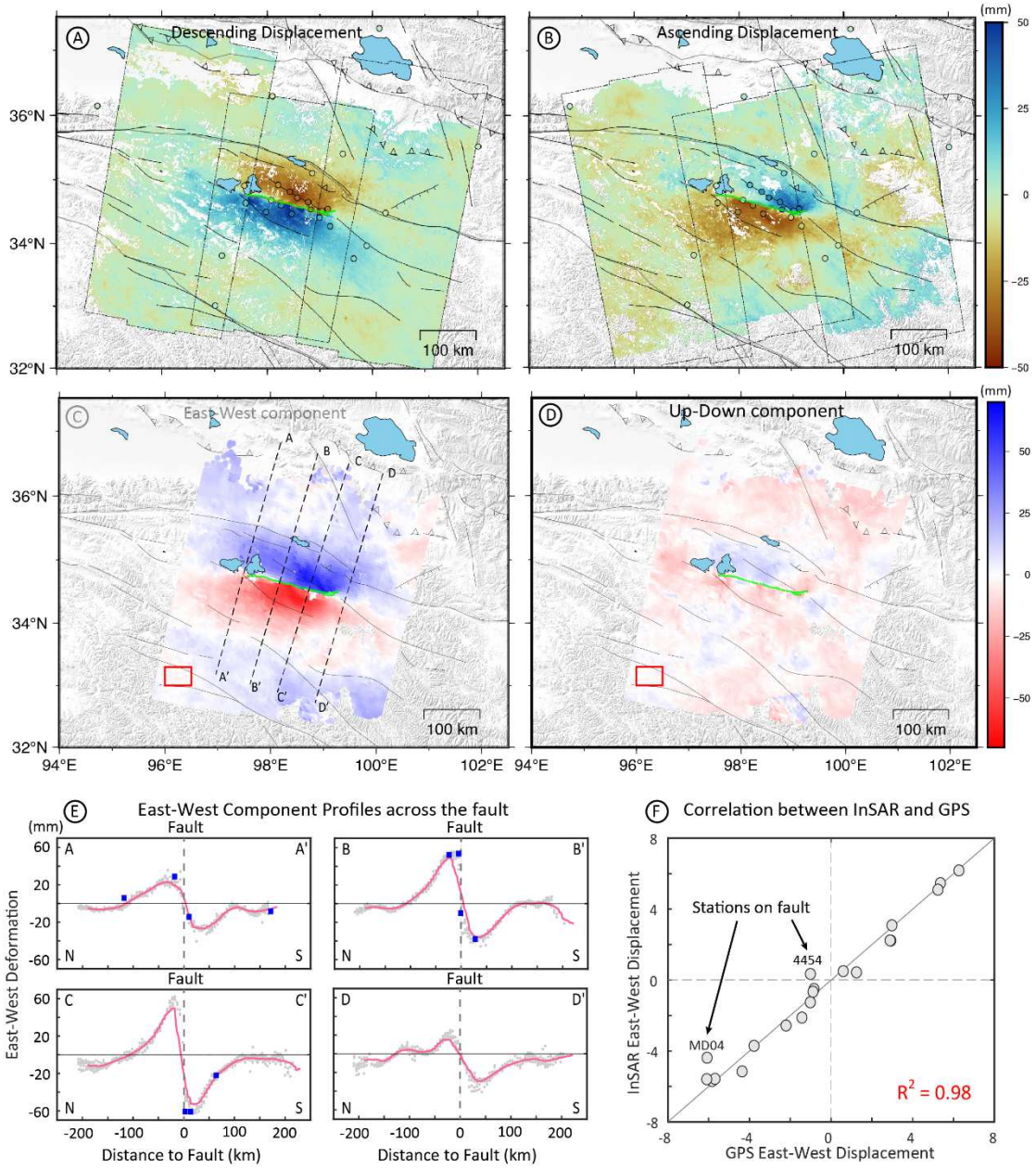

940

941 **Figure 3: InSAR deformation spanning the 2.5 years following the Maduo earthquake**. **(A) (B)**
942 Descending and Ascending Deformation map. The colour-filled dots indicate the GPS
943 accumulative deformation projected in the Line-of-sight direction. **(C) (D)** East-West
944 Component map showing eastward (red) and westward (blue) movements, and Up-Down
945 Component map showing upward (red) and downward (blue) movements. The red rectangle
946 shows the reference area. **(E)** East-West Component Profiles Across the Fault against the
947 distance to the fault. The pink lines indicate the mean value variation along the profiles. Blue
948 squares indicate the GPS accumulative deformation. **(F)** Correlation Between InSAR and GPS:
949 Scatter plot demonstrating a strong correlation (R = 0.98) between east-west displacements
950 measured by InSAR and GPS. Specific stations on the fault, 4454 and MD04, show lower
951 correlation and are not included in the modelling.

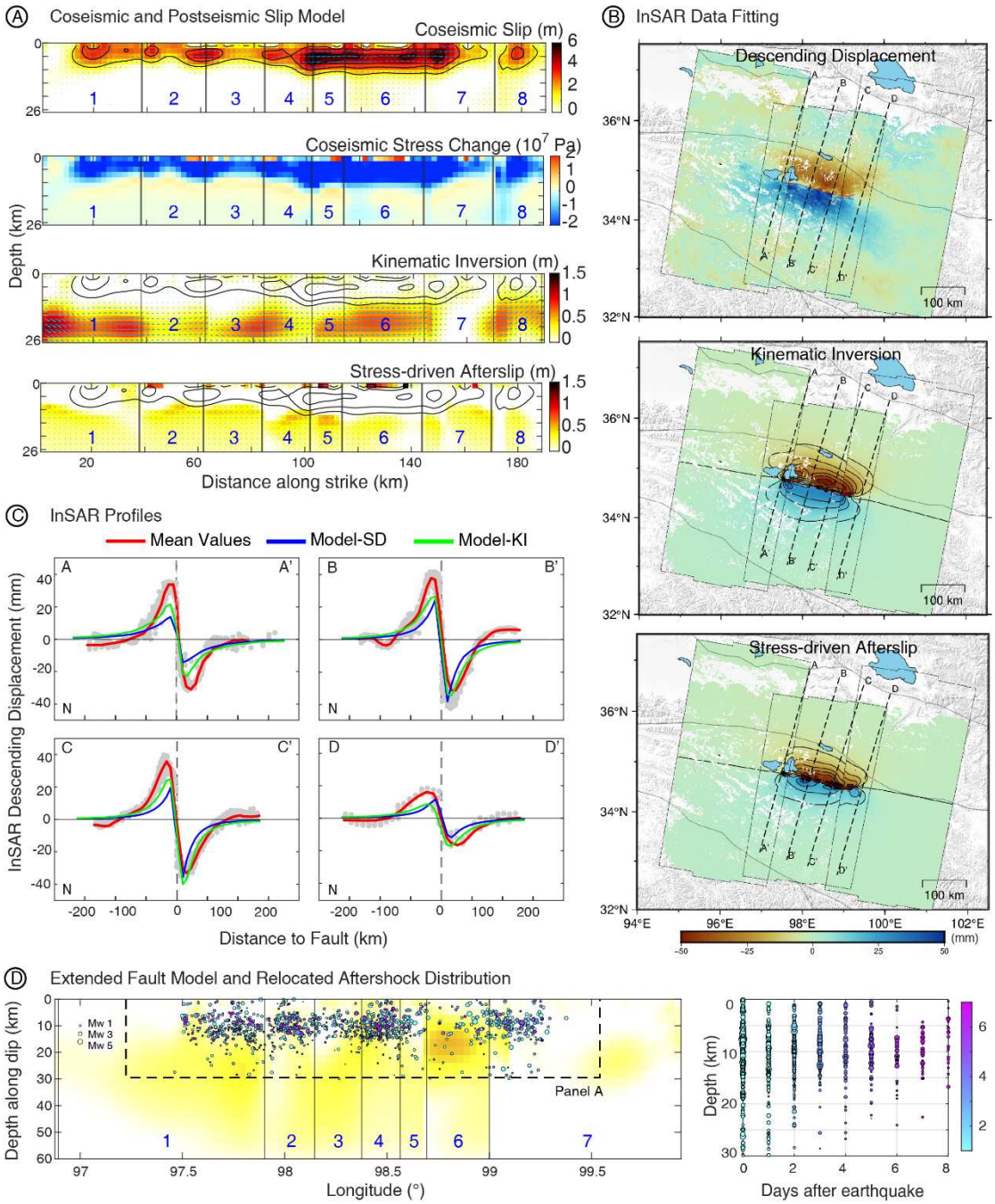

Figure 4: Comparison of kinematic inversion and stress-driven afterslip. (A) Coseismic Slip, Coseismic Stress Change, Kinematic Inversion, and Stress-driven Slip distribution on fault planes. **(B)** Observations of line-of-sight displacements (LOS) and predicted displacements of models from kinematic inversion (RMS: 5.6 mm), and stress-driven slip (RMS: 7.6 mm). **(C)** East-west displacement profiles across the Fault of observed and modelled LOS displacements. **(D)** Left: Depth distribution of kinematically inverted afterslip on extended fault planes, with relocated aftershocks overlain. Most aftershocks cluster near the shallow slip zone (dashed box corresponds to the fault plane in panel A). Right**:** Depth–time distribution of aftershocks within 8 days after the mainshock.

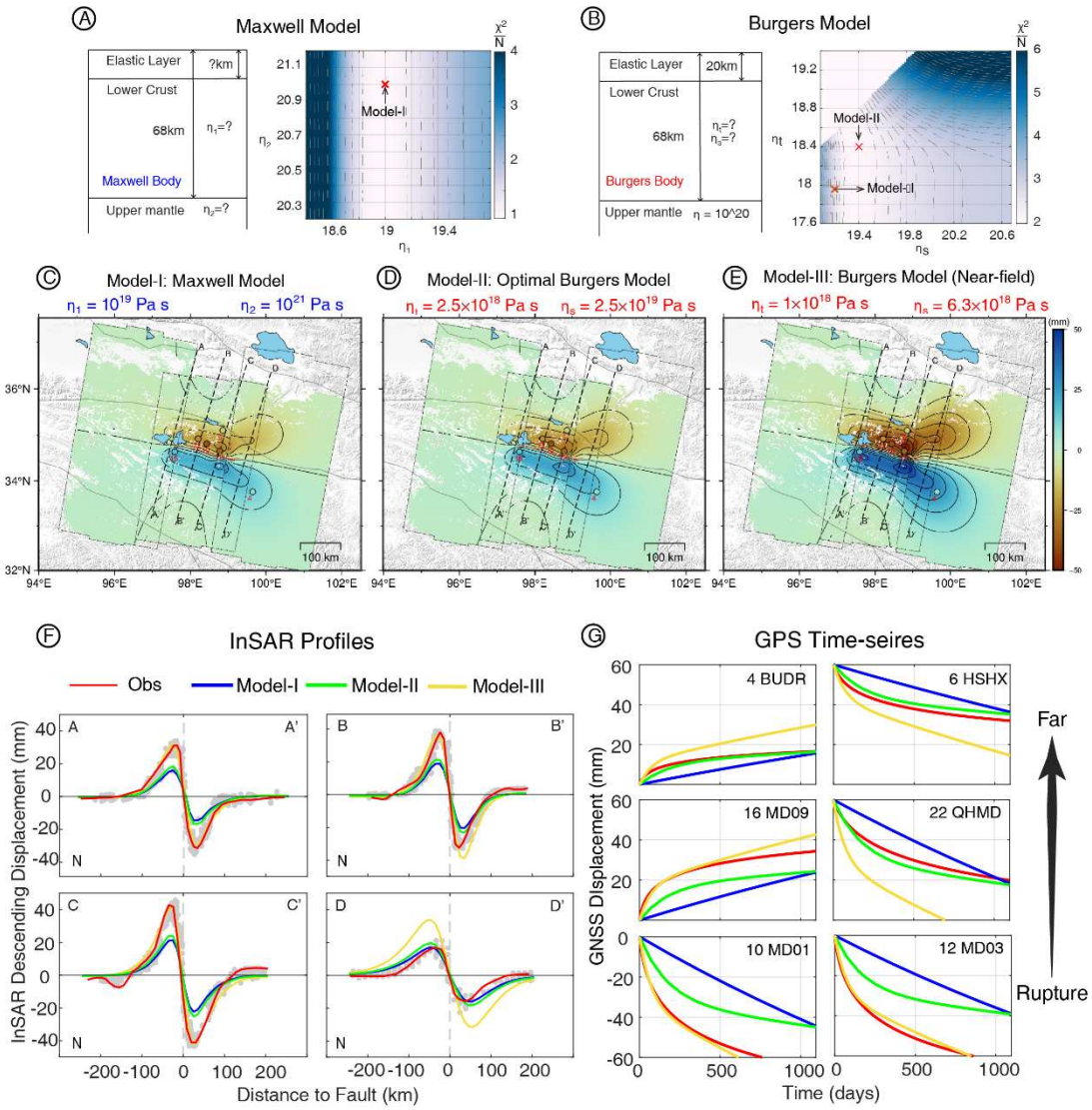

Figure 5: Comparison of Maxwell and Burgers viscoelastic relaxation models. (A) (B) The left maps represent the schematic of the Maxwell Model and Burgers Model, depicting the elastic layer, lower crust (68 km), and upper mantle. The right maps show the misfit maps for the viscosity of the lower crust (η_1) and upper mantle (η_2) for the Maxwell Model, and the misfit maps for transient (η_t) and steady-state (η_s) viscosity for the Burgers Model. **(C)** Model-I (Maxwell Model) shows deformation patterns with $\eta_1 = 10^{19}$ Pa·s and $\eta_2 = 10^{21}$ Pa·s. (RMS: 6.7 mm) **(D)** Model-II (Optimal Burgers Model) illustrates deformation with $\eta_t = 2.5\times10^{18}$ Pa·s and $\eta_s = 2.5\times10^{19}$ Pa·s. (RMS: 6.4 mm) **(E)** Model-III (Burgers Model, Near-field) shows near-field deformation with $\eta_t = 1\times10^{18}$ Pa·s and $\eta_s = 6.3\times10^{18}$ Pa·s. (RMS: 7.1 mm) **(F)** InSAR Displacement Profiles comparing observed (red dashed line) and modelled displacements across four profiles (A-A', B-B', C-C', D-D') using the Model-I (blue line), Model-II (green line), and Model-III (yellow line). **(G)** Comparison between GPS time-series observations and model predictions at stations from far to near the fault.

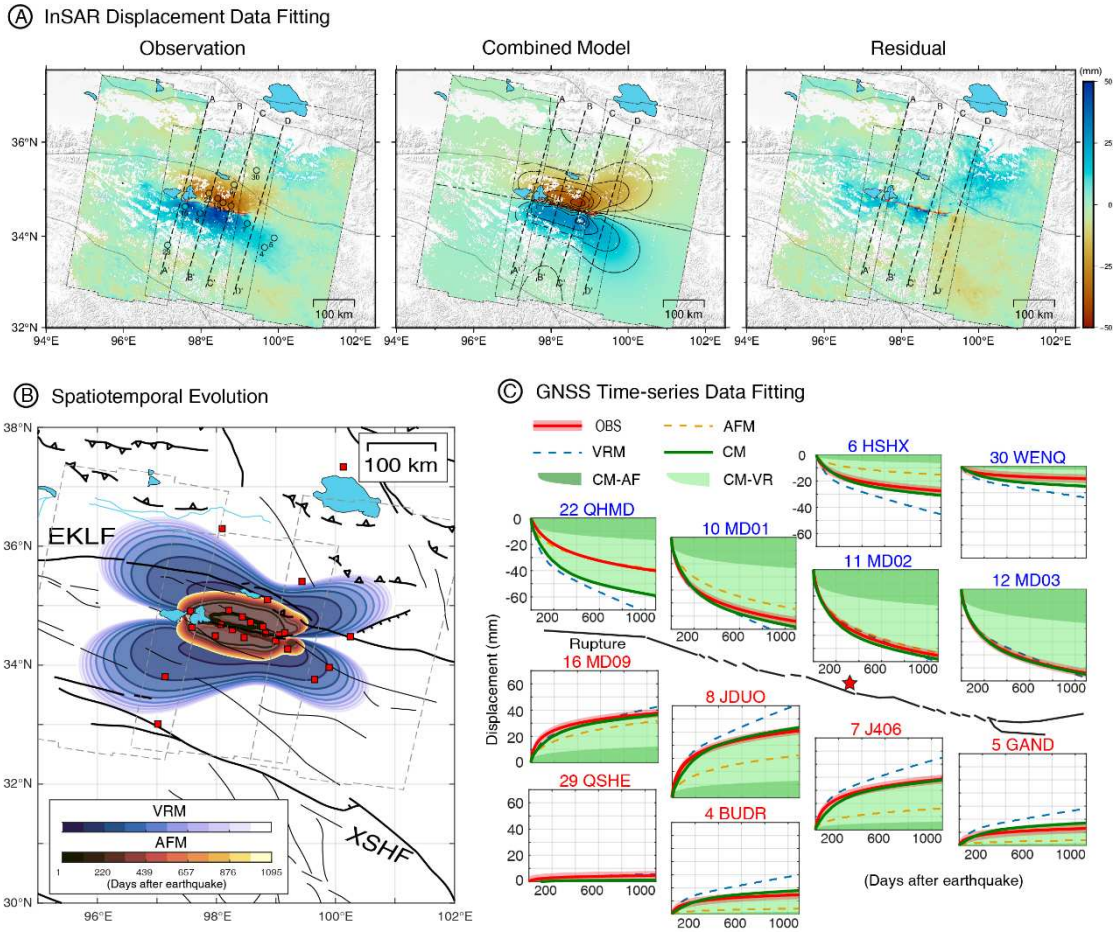

Figure 6. Spatiotemporal evolution and data fitting of the combined postseismic model. (A) InSAR displacement maps showing the observed deformation, predictions from the combined model (afterslip + viscoelastic relaxation), and the residuals (RMS: 5.3 mm). (B) Spatiotemporal evolution of postseismic deformation, indicating the time (in days after the earthquake) required to reach 1.5 cm cumulative displacement from the optimal afterslip and viscoelastic relaxation components. Red squares mark GNSS station locations. (C) GNSS displacement time-series at selected stations, comparing observations (red lines) with the combined model (green), and its individual AFM (rosy brown) and VRM (cyan) components. Green-shaded areas illustrate the contribution of each mechanism: dark green for afterslip (CM-AF) and light green for viscoelastic relaxation (CM-VR). The red-shaded region represents the average uncertainty level of the GNSS time series.

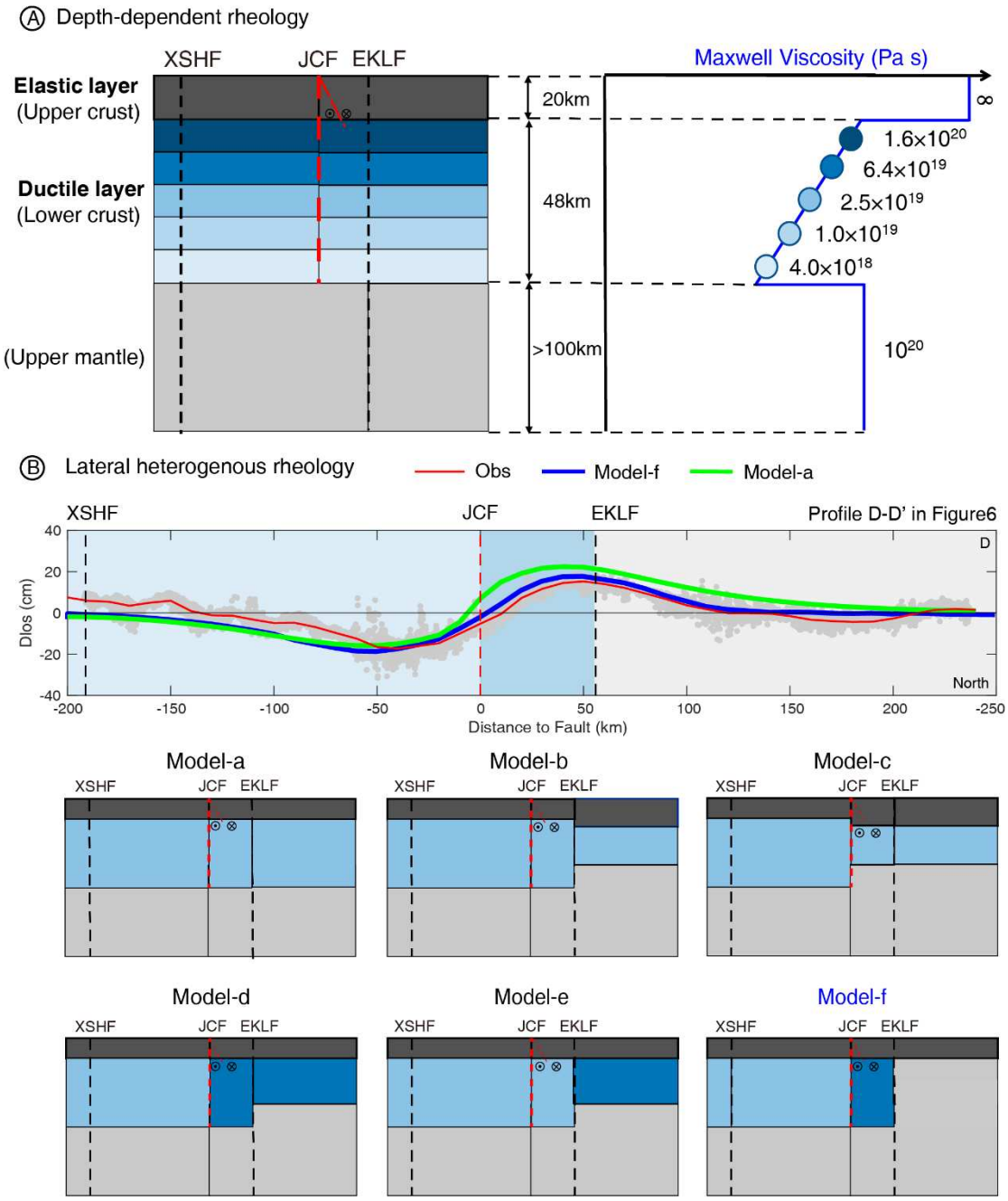

988

989 **Figure 7: Schematic diagram for Depth-dependent and Lateral Heterogeneous Rheology**
990 **Models. (A)** Depth-dependent rheology: Schematic of the lithosphere showing the elastic
991 upper crust and ductile lower crust, with viscosity increasing with depth (blue curve, 1.6×10^{20}
992 Pa·s at the top to 6.3×10^{18} Pa·s at the bottom). **(B)** The upper panel indicates Data fitting along
993 profile D–D′ (indicated in Figure 6). The background shading shows different viscosity. The
994 lower planes indicate lateral heterogeneous rheology: a) basic uniform rheology model, b)
995 variation in elastic layer thickness across the EKLF, c) variation in elastic layer thickness across
996 the JCF, d) an increase in viscosity from the JCF towards the north, e) an increase in viscosity

from the EKLF towards the north, and f) a decrease in viscosity from the JCF towards the south and firm crust north to EKLF. Vertical lines mark fault zones (XSHF, JCF, EKLF), respectively.

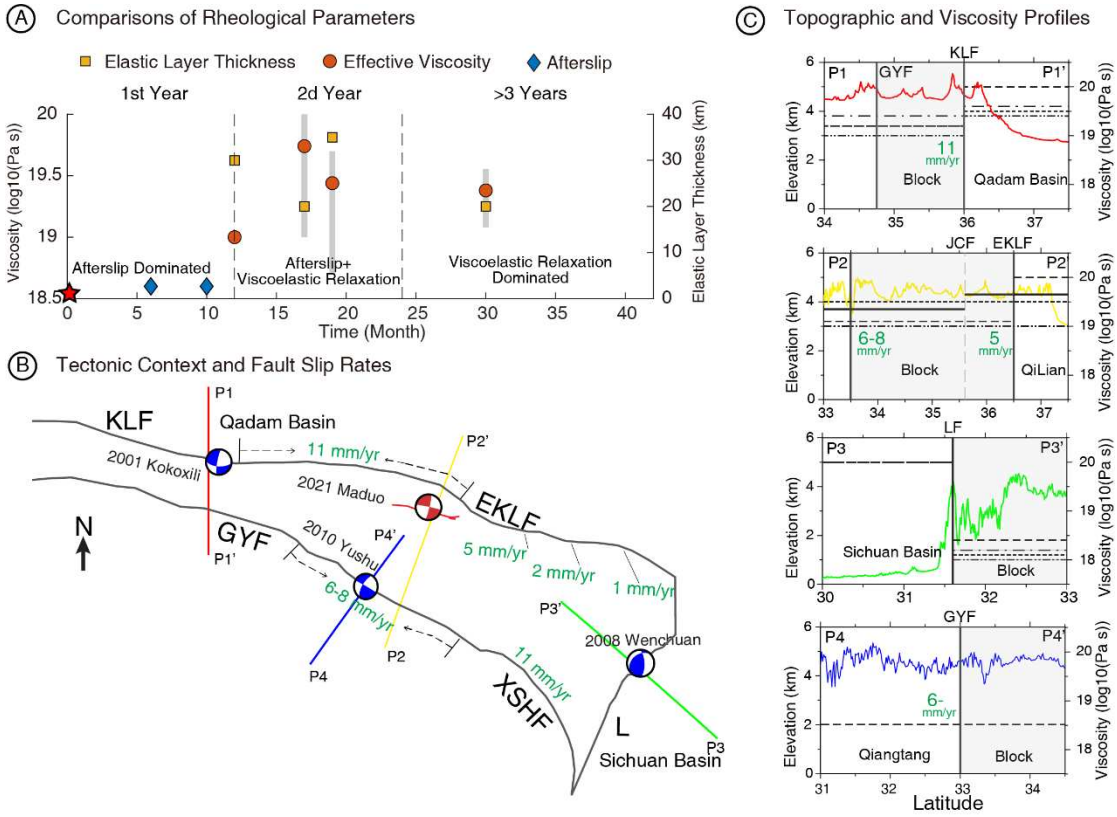

Figure 8: Relationship among crustal rheology, fault slip rates, and topography across tectonic blocks. (A) Comparison with previously published rheological parameters (elastic layer thickness, effective viscosity, and afterslip-dominated deformation) over time following major earthquakes. **(B)** Tectonic map showing major faults (KLF, GYF, EKLF, XSHF) and associated earthquake rupture zones (2001 Kokoxili, 2010 Yushu, 2021 Maduo, 2008 Wenchuan). Labeled slip rates (in mm/yr) are marked along fault segments. Cross-section lines (P1–P4) correspond to the elevation and viscosity profiles shown in panel C. **(C)** Topographic and lower crustal viscosity profiles across four transects. Elevation is plotted against latitude, with corresponding effective viscosity shown on the right axis. The viscosity values represent estimates for the lower crust beneath each transect. Slip rates along each profile are annotated. Different line styles indicate distinct viscosity values as referenced in Tables S3 and S4. Dashed lines represent boundaries between tectonic blocks and sedimentary basins.

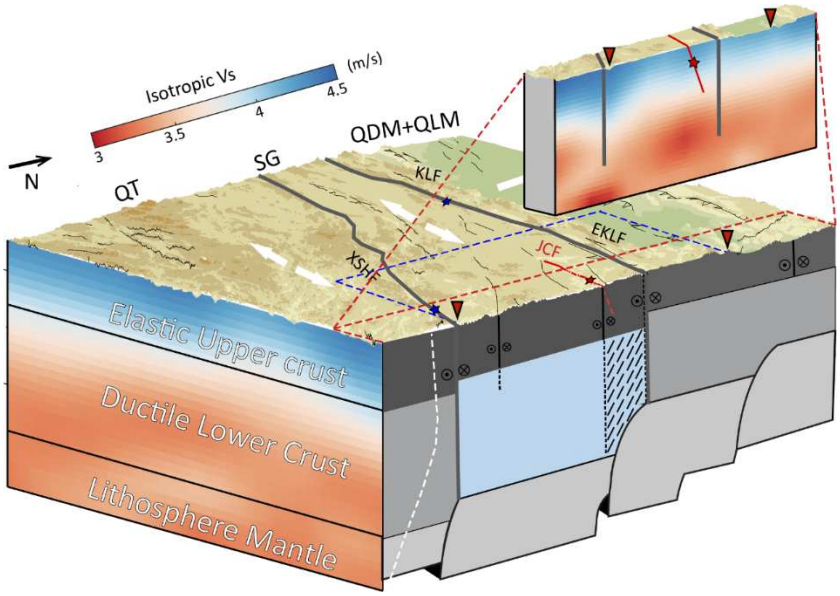

Figure 9: Schematic Diagrams for Regional Tectonic and Crustal Rheology Models. Schematic diagram for the regional tectonic model. The cross-sectional view illustrates the isotropic shear wave velocity (Vs) distribution, differentiating between the elastic upper crust, ductile lower crust, and lithospheric mantle.